

1 Satellite-based radiative forcing by light-absorbing particles in snow across the  
2 Northern Hemisphere

3

4 Jiecan Cui<sup>1</sup>, Tenglong Shi<sup>1</sup>, Yue Zhou<sup>1</sup>, Dongyou Wu<sup>1</sup>, Xin Wang<sup>1, 2</sup> and Wei Pu<sup>1</sup>

5 <sup>1</sup>Key Laboratory for Semi-Arid Climate Change of the Ministry of Education, College

6 of Atmospheric Sciences, Lanzhou University, Lanzhou 730000, China

7 <sup>2</sup>Institute of Surface-Earth System Science, Tianjin University, Tianjin 300072, China

8

9 Corresponding author: Wei Pu (puw09@lzu.edu.cn)

10

1 **Abstract.** Snow is the most reflective natural surface on Earth and consequently plays  
2 an important role in Earth's climate. Light-absorbing particles (LAPs) deposited on the  
3 snow surface can effectively decrease snow albedo, resulting in positive radiative  
4 forcing. In this study, we used remote sensing data from NASA's Moderate Resolution  
5 Imaging Spectroradiometer (MODIS) and the Snow, Ice, and Aerosol Radiative  
6 (SNICAR) model to quantify the reduction in snow albedo due to LAPs, before  
7 validating and correcting the data against in-situ observations. We then incorporated  
8 these corrected albedo-reduction data in the Santa Barbara DISORT Atmospheric  
9 Radiative Transfer (SBDART) model to estimate Northern Hemisphere radiative  
10 forcing except for midlatitude mountains in December-May for the period 2003–2018.  
11 Our analysis reveals an average corrected reduction in snow albedo ( $\Delta\alpha_{MODIS,corrected}^{LAPs}$ )  
12 of  $\sim 0.021$  under all-sky conditions, with daily radiative forcing ( $RF_{MODIS,daily}^{LAPs}$ ) values  
13 of  $\sim 2.9 \text{ W m}^{-2}$ , over land areas with complete or near-complete snow cover and with  
14 little or no vegetation above the snow in Northern Hemisphere. We also observed  
15 significant spatial variations in  $\Delta\alpha_{MODIS,corrected}^{LAPs}$  and  $RF_{MODIS,daily}^{LAPs}$ , with the lowest  
16 respective values ( $\sim 0.016$  and  $\sim 2.6 \text{ W m}^{-2}$ ) occurring in the Arctic and the highest  
17 ( $\sim 0.11$  and  $\sim 12 \text{ W m}^{-2}$ ) in northeastern China. From MODIS retrievals, we determined  
18 that the LAP content of snow accounts for 84% and 70% of the spatial variability in  
19 albedo reduction and radiative forcing, respectively. We also compared retrieved  
20 radiative forcing values with those of earlier studies, including local-scale observations,  
21 remote-sensing retrievals, and model-based estimates. Ultimately, estimates of  
22 radiative forcing based on satellite-retrieved data are shown to represent true conditions

1 on both regional and global scales.

## 2 **1. Introduction**

3 Seasonal snow cover affects 30% of Earth's land surface and exerts a cooling influence  
4 on global climate through its direct interaction with the surface radiances budget  
5 (Painter et al., 1998; Flanner et al., 2011). However, snow surface darkening due to  
6 light-absorbing particles (LAPs) such as black carbon (BC), organic carbon (OC), dust,  
7 and algae, can significantly alter the reflective properties of snow (Warren, 1982, 1984;  
8 Hadley and Kirchstetter, 2012). When deposited on the snow surface, LAPs increase  
9 the absorption of solar radiation (Painter et al., 2012a; Liou et al., 2014; Dang et al.,  
10 2017), thereby reducing the snow albedo (Warren and Brandt, 2008; Kaspari et al.,  
11 2014). As a result, radiative forcing of LAPs in snow (RFLS) plays a critical role in  
12 snow-cover decline on both regional and global scales (Warren and Wiscombe, 1980),  
13 perturbing the climate system and impacting hydrological cycles (Qian et al., 2011).

14 One of the primary LAPs, BC, is derived from the incomplete combustion of fossil  
15 fuels and biomass (Bond et al., 2013; Dang et al., 2015) and is second only to CO<sub>2</sub> in  
16 its contribution to climate forcing (Hansen and Nazarenko, 2004; Ramanathan and  
17 Carmichael, 2008; Bond et al., 2013). Yet, despite considerable efforts to measure the  
18 BC content of Northern Hemisphere snow and ice (Doherty et al., 2010, 2014; Huang  
19 et al., 2011; Ye et al., 2012; Wang et al., 2013b, 2017), the inherent challenges presented  
20 by a temporospatially variable snow cover mean our understanding of LAPs in snow is  
21 far from complete. As a result, persistent uncertainties remain in regional and global-

1 scale RFLS estimates based on field measurements (Zhao et al., 2014).

2 Several previous investigations have utilized numerical models to estimate RFLS,  
3 including that of Hansen and Nazarenko (2004), who concluded that BC in snow and  
4 ice exerts a positive climate forcing throughout the Northern Hemisphere of  $+0.3 \text{ W m}^{-2}$ ,  
5 or explaining approximately one quarter of observed global warming. More recently,  
6 Flanner et al. (2007) employed an aerosol/chemical-transport general-circulation model,  
7 coupled with the Snow, Ice, and Aerosol Radiative (SNICAR) model (Flanner et al.,  
8 2007; 2009), to estimate globally averaged radiative forcing values of  $+0.054$  (range  
9  $0.007\text{--}0.13$ ) and  $+0.049$  ( $0.007\text{--}0.12$ )  $\text{W m}^{-2}$  for a strong (1998) and weak (2001) boreal  
10 fire year, respectively. Using the Weather Research and Forecasting (WRF) model  
11 (Skamarock et al., 2008) coupled with a chemistry component (Chem) (Grell et al.,  
12 2005) and SNICAR modeling, Zhao et al. (2014) demonstrated that RFLS over northern  
13 China in January–February 2010 was  $\sim 10 \text{ W m}^{-2}$ . However, despite their potentially  
14 valuable contribution, climate models contain significant uncertainties in  
15 representations of LAP emissions, transport, deposition, and post-depositional  
16 processes that can propagate into simulations of LAP concentrations and their climate  
17 forcing (Qian et al., 2015; Lee et al., 2016). Zhao et al. (2014) also confirmed that,  
18 relative to observational data, modeled LAPs and radiative forcing estimates exhibit  
19 biases that are difficult to explain and quantify. These shortcomings underscore the need  
20 for a refined approach to estimating real-time RFLS that minimizes the mismatch  
21 between field observations and model simulations.

1 In addition to modeling, remote sensing has been used to assess the physical  
2 characteristics of snow cover (Nolin and Dozier, 1993, 2000; Painter et al., 2009, 2012a,  
3 2013; Miller et al., 2016). Nolin and Dozier (2000), for example, retrieved grain-size  
4 data from satellite-derived reflectance at near-infrared (NIR) wavelengths, following  
5 the rationale that snow-grain size, in conjunction with solar zenith angle, dictates the  
6 path-length of penetrating photons (Wiscombe and Warren, 1980) and thus influences  
7 albedo in the NIR. Similarly, recent studies have attempted to employ satellite-derived  
8 snow albedo at visible (VIS) wavelengths to retrieve RFLS data (Seidel et al., 2016; Pu  
9 et al., 2019). Briefly, this retrieval method exploits the imaginary component of the  
10 complex refractive index for ice ( $K_{ice}$ ), which is very low at VIS wavelengths and  
11 results in the extremely high VIS albedo for pure snow. In contrast, the imaginary  
12 component of the complex refractive index for LAPs ( $K_{LAPs}$ ) at VIS wavelengths is  
13 orders of magnitude greater, resulting in the reduction in VIS snow albedo (Wiscombe  
14 and Warren, 1980). Moreover, albedo variability at VIS wavelengths is dominated by  
15 even minor concentrations of LAPs (Brandt et al., 2011; Painter et al., 2012b).

16 Painter et al. (2012a) employed surface-reflectance data provided by NASA's Moderate  
17 Resolution Imaging Spectroradiometer (MODIS) for the Upper Colorado River Basin  
18 and Hindu Kush-Himalaya (HKH) to make the first quantitative, remote-sensing-based  
19 retrievals of instantaneous surface radiative forcing (RF) due to LAPs. Relative to the  
20 Western Energy Balance of Snow (WEBS) network (Painter et al., 2007), that study  
21 established that MODIS-derived radiative forcing exhibits a positive bias at lower RF

1 values and a slightly negative bias at higher values. A more recent study by Seidel et al.  
2 (2016) used remote sensing to constrain instantaneous melt-season RFLS values of 20–  
3 200 W m<sup>-2</sup> for the Sierra Nevada and Rocky Mountains, while Pu et al. (2019) reported  
4 MODIS-derived values of 22–65 W m<sup>-2</sup> for northern China in January–February  
5 (regional average ~45 W m<sup>-2</sup>). Acknowledging this demonstrated efficacy of remote  
6 sensing retrievals for establishing RFLS on regional scales, we note this approach has  
7 so far not captured spatial variability in RFLS on a global scale.

8 In this study, we employed MODIS data to determine the reduction in Northern  
9 Hemisphere snow albedo due to LAPs. Retrievals were validated and corrected  
10 according to ground-based snow observations, after which spatial variability in albedo  
11 reduction and radiative forcing over mapped snow-covered area in Northern  
12 Hemisphere were assessed quantitatively. Finally, we compared our satellite-derived  
13 radiative forcing values with the modeling results of CESM2 (Eyring et al., 2016;  
14 Danabasoglu et al., 2020). Despite the persistence of non-negligible uncertainties and  
15 biases, our satellite-based retrievals constitute the first hemisphere-scale assessment of  
16 RFLS and provide valuable information for improving climate model simulations.

## 17 **2. Data**

### 18 **2.1. Remote-sensing data**

19 To investigate the impact of LAPs on snow albedo, we utilized the following MODIS  
20 data sets: surface albedo (MCD43C3; 0.05° × 0.05° resolution), snow cover  
21 (MYD10C1; 0.05° × 0.05° resolution), land cover type (MCD12C1; 0.05° × 0.05°

1 resolution), and atmospheric parameters (MYD08\_D3;  $1^\circ \times 1^\circ$  resolution). Each data  
2 set corresponds to December-May for the period 2003–2018 (<https://earthdata.nasa.gov>,  
3 last access: 20 January 2019). MCD43C3 is the daily combined MODIS output derived  
4 from both the Terra and Aqua satellites, and provides black-sky albedo (directional  
5 hemispherical reflectance, DHF) and white-sky albedo (bi-hemispherical reflectance,  
6 BHF) at local solar noon for bands 1–7 (band 1, 620–670 nm; band 2, 841–876 nm;  
7 band 3, 459–479 nm; band 4, 545–565 nm; band 5, 1230–1250 nm; band 6, 1628–1652  
8 nm; band 7, 2105–2155 nm), as well as values for quality control, local noon solar  
9 zenith angle, and associated parameters. MCD43C3 observations are weighted to  
10 estimate albedo on the 9th day of each 16-day period and have been corrected for the  
11 influence of local slope and aspect, atmospheric gases, and aerosols.

12 Snow-cover data are provided daily by MYD10C1 as a report of the snow-cover  
13 fraction (SCF), derived from the Normalized Difference Snow Index (NDSI).  
14 MCD12C1 provides a spatially aggregated and reprojected land-cover type, which is  
15 derived from the supervised classification of MODIS reflectance data, while MODIS  
16 MYD08\_D3 reports values of solar azimuth angle.

17 Average-daily solar radiances and cloud fraction were obtained from NASA's Clouds  
18 and the Earth's Radiant Energy System (CERES: <https://ceres.larc.nasa.gov>, last access:  
19 12 April 2019), part of the Earth Observing System comprising the Aqua, Terra, and S-  
20 NPP satellites. CERES provides instantaneous measurements of solar radiances, which  
21 are then converted to average-daily flux by angular dependence and empirical diurnal

1 albedo modeling as the satellite passes through the point of descent (Doelling et al.,  
2 2013; Su et al., 2015; Loeb et al., 2018). We used the total downward shortwave flux  
3 and cloud fraction at the surface, provided by the “CERES Single Scanner Footprint  
4 1.08 (SSF1deg)” product, to estimate average-daily RFLS under all-sky conditions.  
5 Shuttle Radar Topography Mission (SRTM) digital elevation data are provided by the  
6 US Geological Survey (<https://www.usgs.gov/>, last access: 9 December 2018) to adjust  
7 slope- and aspect-induced changes of surface solar irradiance in complex terrain. The  
8 spatial resolution of SRTM data for the Northern Hemisphere is 30 m.

## 9 **2.2. Snow depth data**

10 Estimates of snow depth were obtained from the European Centre for Medium-Range  
11 Weather Forecasts (ECMWF) Interim Re-Analysis (ERA-Interim)  
12 (<https://www.ecmwf.int>, last access: 15 January 2019). ERA-Interim is a new  
13 generation of reanalysis based on a 12-hourly and 4-dimensional variational data  
14 assimilation (4D-Var) covering the period 1979–present. ERA-Interim performs better  
15 in model physics frameworks, data quality control, and background error criteria than  
16 previous versions (Berrisford et al., 2011; Brun et al., 2013). In this study, we used  
17 snow-water equivalent (SWE) data for December-May covering the period 2003–2018.  
18 These data were generated by forecast models and updated according to a Cressman  
19 analysis of snow observations (Drusch et al., 2004; Dee et al., 2011). We note that the  
20 previous occurrence of false snow-free patches, arising from application of Cressman  
21 analysis in regions of sparse ground control, has been mitigated by ECMWF upgrades



1 (Dee et al., 2011). Finally, SWE is converted to snow depth by assuming that average  
2 December-May snow density is  $\sim 300 \text{ kg m}^{-3}$ , consistent with snow-depth estimates by  
3 the Canadian Meteorological Centre (CMC) (Sturm et al., 1995; Brown and Mote,  
4 2009).

### 5 **2.3. In-situ measurements of LAPs in snow**

6 To correct the satellite retrievals, we collected a comprehensive set of in-situ  
7 measurements of BC concentrations from the field campaigns in the Arctic in spring of  
8 2005-2009 (Doherty et al., 2010), North America in January-March of 2013 (Doherty  
9 et al., 2014), Northern China in January-February of 2010, 2012 and 2014 (Ye et al.,  
10 2012; Wang et al., 2013; Wang et al., 2017). The BC concentrations are measured by  
11 the two-sphere integrating-sandwich (TSI) spectrophotometer in the Arctic, North  
12 America, and Northern China (Grenfell et al., 2011; Wang et al., 2020). Briefly, TSI  
13 produces a diffuse radiation field when the white light illumination is transmitted into  
14 an integrating sphere; then the diffuse radiation passes through the filter and is detected  
15 by a spectrometer. The TSI technique acquires the light attenuation spectrum due to the  
16 LAPs loaded on the sample filter (Grenfell et al., 2011). Then, the light attenuation  
17 spectrum of the sample filter is transformed into an equivalent BC mass (unit:  $\text{g cm}^{-2}$ )  
18 loading by comparing against the standard filters. The equivalent BC has been defined  
19 by Doherty et al. (2010) which briefly as the amount of BC in the snow accounted for  
20 the wavelength-integrated total light absorption in the wavelengths of 300-750 nm by  
21 all particulate constituents. In this study, we used  $BC_{equiv}$  for all LAPs to calculate the

1 in-situ snow albedo reduction and radiative forcing (Fig. S3).

## 2 **2.4. Climate model simulations**

3 We compared our remotely sensed retrievals of daily-average RFLS for the 2003–2014  
4 study period with simulated results derived from CESM2 (<https://esgf-node.llnl.gov/>,  
5 last access: 15 July 2019). In this study, we employed simulations of snow BC  
6 concentrations derived from the CESM2 historical experiments, in conjunction with  
7 ERA-Interim SWE, MODIS-retrieved snow grain-size, and CERES total downward  
8 shortwave flux data under all-sky condition, to model daily-average RFLS for the study  
9 period. Simulations were performed using the Snow, Ice, and Aerosol Radiative  
10 (SNICAR) and Santa Barbara DISORT Atmospheric Radiative Transfer (SBDART)  
11 models, and the model output was compared with satellite-based retrievals.

## 12 **3. Methods**

### 13 **3.1. Radiative transfer model**

14 In this study, we used the Santa Barbara DISORT Atmospheric Radiative Transfer  
15 (SBDART) model to calculate spectral surface solar irradiance. Constituting one of the  
16 most widely applied models for calculating the atmospheric radiative transfer at Earth's  
17 surface, under both clear- and cloudy-sky conditions (Ricchiazzi et al., 1998), SBDART  
18 combines a low-resolution atmospheric transmission model, Discrete Ordinate  
19 Radiative Transfer (DISORT) module, and Mie scattering output for the scattering of  
20 light by ice crystals and water droplets (Stamnes et al., 1988; Fu et al., 2017). Radiative  
21 transfer equations for a vertically inhomogeneous, non-isothermal, plane-parallel

1 atmosphere are integrated numerically using the DISORT module. SBDART comprises  
2 multiple standard atmospheric profiles, cloud models, basic surface types, as well as  
3 vertical distribution models for aerosols and gas absorption, and enables users to specify  
4 these input parameters in real values. In our study, the subarctic and midlatitude winter  
5 standard atmospheric condition are assumed as well as the tropospheric and  
6 stratospheric background aerosols are archived in SBDART (Tanre, D. et al., 1990).  
7 According to Dang et al. (2017), the cloud optical depth in high-latitude and mid-  
8 latitude was assumed as 11 and 20 under cloudy-sky condition, respectively. The  
9 spectral irradiance from SBDART is only used for integrating the spectral MODIS  
10 albedo to achieve broadband albedo, thus the uncertainty of solar irradiance from the  
11 assumed atmospheric properties has limited influence on the retrieval of radiative  
12 forcing (see Section 3.2). Average incident direct and diffuse solar spectra for  
13 December-May under clear/cloudy sky are shown in Fig. S1.

14 The Snow, Ice, and Aerosol Radiative (SNICAR) model is a two-stream multiple  
15 scattering radiative transfer model (Flanner et al., 2007, 2009) that has been used widely  
16 both to simulate the albedo, transmission, and vertical absorptivity of LAP-  
17 contaminated snowpack and to estimate RFLS (Painter et al., 2012a; Bryan et al., 2013;  
18 Miller et al., 2016). SNICAR employs the theory proposed by Wiscombe and Warren  
19 (1980) and Toon et al. (1989). Specifically, snow is considered to be composed of  
20 aggregated ice grains with optical effective radii ( $R_{eff}$ ) of 50–1500  $\mu\text{m}$ , lognormal  
21 distribution, and spherical grain shape. SNICAR also accounts for the incident radiation

1 at the surface and its spectral distribution, solar zenith angle, snow depth and density,  
2 snow layer number, and the type and concentration of LAPs in the snowpack. The  
3 model's ability to provide realistic simulations of snow albedo has been verified by  
4 several previous studies (Hadley and Kirchstetter, 2012; Meinander et al., 2013; Zhong  
5 et al., 2017; Wang et al., 2017).

### 6 **3.2. Retrieval of quantitative snow properties from remote sensing**

7 The variability of spectral snow albedo depends on the LAP content, grain size, grain  
8 shape, and depth of the snowpack, in addition to solar zenith angle. As shown in Fig.  
9 1a, the deposition of BC (as representative of LAPs generally) serves to decrease the  
10 albedo of snow significantly, particularly in the ultraviolet (UV) and VIS wavelengths,  
11 which account for approximately half of all direct solar irradiance and the majority of  
12 diffuse solar irradiance (Fig. S1). In contrast, the impact of BC on albedo is  
13 considerably smaller in NIR wavelengths and can be negligible at  $> \sim 1150$  nm. Snow  
14 depth plays a similar role to LAP content and primarily affects albedo in UV and VIS  
15 wavelengths (Fig. 1b).

16 Although snow albedo decreases with snow depth, previous studies have tended to  
17 assume a semi-infinite snowpack for which albedo is independent of depth. As a  
18 consequence, the role of LAPs in albedo reduction has been overestimated for those  
19 areas where the snowpack is thin (Warren, 2013). In this study, we incorporated ERA-  
20 Interim SWE data in our SNICAR model simulations to correct for the snow-depth  
21 overestimation effect. In contrast, snow grain-size and solar zenith angle influence the

1 snow albedo chiefly in NIR wavelengths (Fig. 1c, d). Specifically, albedo tends to  
 2 decrease with increasing snow grain-size and declining solar zenith angle. In this study,  
 3 we derived quantitative snow parameters (grain size, albedo reduction, and RFLS) from  
 4 MODIS data in conjunction with the SNICAR and SBDART models. The specific  
 5 workflow for retrieving RFLS from satellite data is shown in Fig. 2.

### 6 **3.2.1. Retrieval of blue-sky albedo**

7 MCD43 provides black-sky and white-sky albedo, which are defined as albedo in the  
 8 absence of diffuse and direct component of solar irradiance. Accordingly, the actual  
 9 spectral albedo for a land surface at wavelength  $\lambda$  (also called blue-sky albedo:  
 10  $\alpha_{MODIS,\lambda}^{blue-clear}$ ) under clear-sky condition can be calculated as follows:

$$11 \quad \alpha_{MODIS,\lambda}^{blue-clear} = f_{dif,\lambda}^{clear} \cdot \alpha_{MODIS,\lambda}^{white-sky} + (1 - f_{dif,\lambda}^{clear}) \cdot \alpha_{MODIS,\lambda}^{black-sky} \quad (1)$$

12 where  $\alpha_{MODIS,\lambda}^{white-sky}$  and  $\alpha_{MODIS,\lambda}^{black-sky}$  are MODIS-derived values for white-sky and  
 13 black-sky albedo, respectively, and  $f_{dif,\lambda}^{clear}$  is the ratio of diffuse irradiance to the total  
 14 solar irradiance under clear-sky (Lewis and Barnsley, 1994). The latter is calculated as  
 15 follows:

$$16 \quad f_{dif,\lambda}^{clear} = \frac{E_{dif}^{clear}(\lambda; \varphi)}{E_{dif}^{clear}(\lambda; \varphi) + E_{dir}^{clear}(\lambda; \varphi) \cdot \cos\beta} \quad (2)$$

17 where  $\varphi$  is latitude, and  $E_{dif}^{clear}(\lambda; \varphi)$  denote the diffuse spectral irradiance on a  
 18 horizontal surface and  $E_{dir}^{clear}(\lambda; \varphi)$  denote the direct spectral irradiance on a surface  
 19 perpendicular to the sun, derived from the SBDART model under clear-sky condition.  $\beta$   
 20 represents local solar zenith angle, which is obtained using the topographic correction

1 method (Teillet et al., 1982; Negi and Kokhanovsky, 2011):

$$2 \quad \cos \beta = \cos \theta_0 \cos \theta_T + \sin \theta_0 \sin \theta_T \cos(\phi_0 - \phi_T) \quad (3)$$

3 for which  $\theta_0$  represents the solar zenith angle for a horizontal surface,  $\phi_0$  is the solar  
4 azimuth angle, and  $\theta_T$  and  $\phi_T$  denote slope inclination and aspect, respectively.

5 Similarly, we can derive the blue-sky albedo for cloudy-sky condition ( $\alpha_{MODIS,\lambda}^{blue-cloudy}$ ).

6 Then, we used cloud fraction ( $f_{cloud}$ ) from CERES to weight clear-sky albedo and  
7 cloudy-sky albedo to obtain actual all-sky albedo ( $\alpha_{MODIS,\lambda}^{all}$ ):

$$8 \quad \alpha_{MODIS,\lambda}^{all} = f_{cloud} \cdot \alpha_{MODIS,\lambda}^{blue-cloudy} + (1 - f_{cloud}) \cdot \alpha_{MODIS,\lambda}^{blue-clear} \quad (4)$$

### 9 **3.2.2. Retrieval of snow cover and albedo values**

10 As shown in Fig. 2, the snow-covered area is mapped according to the actual all-sky  
11 albedo ( $\alpha_{MODIS,\lambda}^{all}$ ) in band 4 (band center ~555 nm) and the Normalized Difference  
12 Snow Index (NDSI), both of which are required to exceed 0.6 (Negi and Kokhanovsky,  
13 2011). According to the MODIS Snow Products Collection 6 User Guide  
14 (<http://nsidc.org/data>), the Fractional Snow Cover ( $FSC$ ) can be calculated as follows:

$$15 \quad FSC = -0.01 + 1.45 \cdot NDSI \quad (5)$$

16 Accordingly, the identified snow-covered area (ISCA) has an  $FSC$  value of >86% but  
17 not always 100%. Therefore, the MODIS-derived albedo for a particular ISCA is a  
18 combination of values representing both snow and the snow-free underlying surface.  
19 Following Pu et al. (2019), the snow albedo ( $\alpha_{snow,\lambda}^{all}$ ) can be distinguished from the  
20 mixed albedo by the equation:

$$\alpha_{MODIS,\lambda}^{all} = \frac{E_{all-sky,\lambda} \cdot FSC \cdot \alpha_{snow,\lambda}^{all} + E_{all-sky,\lambda} \cdot (1 - FSC) \cdot \alpha_{underlying,\lambda}}{E_{all-sky,\lambda}}$$

$$= FSC \cdot \alpha_{snow,\lambda}^{all} + (1 - FSC) \cdot \alpha_{underlying,\lambda} \quad (6)$$

$$\alpha_{snow,\lambda}^{all} = \frac{\alpha_{MODIS,\lambda}^{all} - (1 - FSC) \cdot \alpha_{underlying,\lambda}}{FSC} \quad (7)$$

where  $E_{all-sky,\lambda}$  is total solar irradiance under all-sky condition, a linear combination of direct/diffuse component of solar irradiance under clear-sky and cloudy-sky using similar strategy via Eq. (1)-(4).  $\alpha_{underlying,\lambda}$  represents the albedo of the underlying surface and was obtained from Siegmund and Menz (2005). As depicted in Fig. 3b, vegetation and bare soil are the main types of underlying surface in the ISCA.

### 3.2.3. Retrieval of snow grain size

The snow optical-equivalent grain size ( $R_{eff}$ ) is retrieved by fitting SNICAR-simulated snow albedo to MODIS-derived snow albedo at 1240 nm (the central wavelength of MODIS band 5), following the protocol of Nolin and Dozier (2000). This retrieval method is not influenced by liquid water and water vapor and has been employed widely in previous studies (e.g., Painter et al., 2013; Seidel et al, 2016). Both Nolin and Dozier (2000) and Pu et al. (2019) reported that the retrieved  $R_{eff}$  compares favorably with ground-based measurements of snow grain size. In this study, we chose to exclude the ISCA, where MODIS-derived snow albedo at 1240 nm is <0.3, to avoid misrepresenting  $R_{eff}$  (Tedesco et al., 2007).

### 3.2.4. Retrieval of snow albedo reduction and RFLS

The spectrally integrated reduction in snow albedo due to LAPs ( $\Delta\alpha_{MODIS,noon}^{LAPs}$ ) is

1 estimated for local-noon and all-sky conditions, using solar irradiance and the  
 2 difference between MODIS-derived spectral snow albedo ( $\alpha_{snow,\lambda}^{all}$ ) and simulated pure  
 3 snow albedo ( $\alpha_{snow,\lambda}^{mdl}$ ). Because MODIS provides only four VIS bands, we fitted snow  
 4 albedo data obtained via MODIS to a continuous 300–2500 nm spectrum ( $\alpha_{snow,\lambda}^{MODIS}$ , with  
 5 a 10 nm interval) following the method provided by Pu et al. (2019). Thereafter, the  
 6 broadband albedo reduction due to LAPs retrieved from MODIS ( $\Delta\alpha_{MODIS,noon}^{LAPs}$ ) can  
 7 be calculated as follows:

$$8 \quad \Delta\alpha_{MODIS,noon}^{LAPs} = \frac{\sum_{\lambda=300nm}^{\lambda=2500nm} (\alpha_{snow,\lambda}^{mdl} - \alpha_{snow,\lambda}^{MODIS}) \cdot E_{all-sky,\lambda} \cdot \Delta\lambda}{\sum_{\lambda=300nm}^{\lambda=2500nm} E_{all-sky,\lambda} \cdot \Delta\lambda} \quad (8)$$

9 where  $\alpha_{snow,\lambda}^{mdl}$  is the pure snow albedo simulated by SNICAR using MODIS-derived  
 10  $R_{eff}$  and ERA-Interim snow depth data,  $\alpha_{snow,\lambda}^{MODIS}$  is the continuous snow albedo  
 11 derived from MODIS retrievals, and  $\Delta\lambda$  is 10 nm.

12 Following Miller et al. (2016), we assumed that the properties for snow and LAPs  
 13 remain invariable throughout the day. Based on calculated  $\alpha_{snow,\lambda}^{mdl}$  and  $\alpha_{snow,\lambda}^{MODIS}$  at  
 14 noon, the diurnal variation of pure and polluted snow albedo can be simulated by  
 15 SNICAR from sunrise to sunset. Then, daily-average snow albedo reduction  
 16 ( $\Delta\alpha_{MODIS,daily}^{LAPs}$ ) can be derived by integrating the diurnal snow albedo reduction, which  
 17 is weighted by simultaneous solar irradiance from SBDART. Similarly, we used  
 18 measurements of LAPs in contaminated snow to calculate the  
 19 in-situ reduction in snow albedo ( $\Delta\alpha_{in-situ,daily}^{LAPs}$ ). To derive a correction factor for  
 20 MODIS retrievals, we applied a similar validation strategy to that of Zhu et al. (2017):



$$c = \frac{1}{n} \sum_{i=1}^n \left( \frac{\Delta\alpha_{MODIS,daily}^{LAPs}}{\Delta\alpha_{in-situ,daily}^{LAPs}} \right) \quad (9)$$

where  $c$  is the correction factor for  $\Delta\alpha_{MODIS,daily}^{LAPs}$  and  $n$  is the number of the respective in-situ measurements. Accordingly, the corrected albedo reduction ( $\Delta\alpha_{MODIS,corrected}^{LAPs}$ ) is calculated as follows:

$$\Delta\alpha_{MODIS,corrected}^{LAPs} = \frac{1}{c} \cdot \Delta\alpha_{MODIS,daily}^{LAPs} \quad (10)$$

The daily-average, spectrally integrated RFLS ( $RF_{MODIS,daily}^{LAPs}$ ) is calculated for all-sky conditions as follows:

$$RF_{MODIS,daily}^{LAPs} = \Delta\alpha_{MODIS,corrected}^{LAPs} \cdot SW_{all-sky} \quad (11)$$

where  $SW_{all-sky}$  represent the average-daily total downward shortwave fluxes, obtained from CERES under all-sky conditions.

### 3.2.5. Attribution of spatial variability in snow albedo reductions and radiative forcing

As demonstrated above, reductions in snow albedo and RFLS are dependent primarily on LAP content,  $R_{eff}$ , snow depth ( $SD$ ), solar zenith angle, surface topography, and solar irradiance, the latter three of which can be categorized as the geographic factor ( $G$ ). We used an impurity index ( $I_{LAPs}$ ) to represent the LAP content of the snowpack (Di Mauro et al., 2015; Pu et al., 2019), following the equation:

$$I_{LAPs} = \frac{\ln(\alpha_{snow,band4}^{all})}{\ln(\alpha_{snow,band5}^{all})} \quad (12)$$

where  $\alpha_{snow,band4}^{all}$  and  $\alpha_{snow,band5}^{all}$  are the MODIS-derived snow albedo values for bands 4 and 5, respectively. We then calculated  $\Delta\alpha_{MODIS,corrected}^{LAPs}$  as follows:

$$\Delta\alpha_{MODIS,corrected}^{LAPs} = f(I_{LAPs}, R_{eff}, SD, G) \quad (13)$$

The spatial variability in snow albedo reduction due to  $I_{LAPs}$  can be expressed as

$$\Delta\alpha_{MODIS,corrected}^{LAPs}(I_{LAPs}) = f(I_{LAPs}, \overline{R_{eff}}, \overline{SD}, \overline{G}) \quad (14)$$

where  $\overline{R_{eff}}, \overline{SD}, \overline{G}$  indicate spatial-mean values of  $R_{eff}, SD$ , and  $G$ , with  $\overline{G}$  requiring spatially constant values for the solar zenith angle, surface topography, and solar irradiance parameters. The following three equations were applied in a similar manner:

$$\Delta\alpha_{MODIS,corrected}^{LAPs}(R_{eff}) = f(\overline{I_{LAPs}}, R_{eff}, \overline{SD}, \overline{G}) \quad (15)$$

$$\Delta\alpha_{MODIS,corrected}^{LAPs}(SD) = f(\overline{I_{LAPs}}, \overline{R_{eff}}, SD, \overline{G}) \quad (16)$$

$$\Delta\alpha_{MODIS,corrected}^{LAPs}(G) = f(\overline{I_{LAPs}}, \overline{R_{eff}}, \overline{SD}, G) \quad (17)$$

We then fitted  $\Delta\alpha_{MODIS,corrected}^{LAPs}$  through multiple linear regression:

$$\Delta\alpha_{MODIS}^{LAPs,fit} = a \cdot \Delta\alpha_{MODIS,corrected}^{LAPs}(I_{LAPs}) + b \Delta\alpha_{MODIS,corrected}^{LAPs}(R_{eff}) + c \cdot \Delta\alpha_{MODIS,corrected}^{LAPs}(SD) + d \cdot \Delta\alpha_{MODIS,corrected}^{LAPs}(G) \quad (18)$$

where  $\Delta\alpha_{MODIS}^{LAPs,fit}$  is the fitted snow albedo reduction and a, b, c, and d denote the regression coefficients. Figure S3a illustrates how  $\Delta\alpha_{MODIS}^{LAPs,fit}$  can explain 99% of the variance in  $\Delta\alpha_{MODIS,corrected}^{LAPs}$ . Therefore, the attribution of spatial variance in  $\Delta\alpha_{MODIS,corrected}^{LAPs}$  can be replaced with  $\Delta\alpha_{MODIS}^{LAPs,fit}$ , enabling Eq. (18) to be written as follows:

$$\Delta\alpha_{MODIS}^{LAPs,fit} - \overline{\Delta\alpha_{MODIS}^{LAPs,fit}} = a \cdot (\Delta\alpha_{MODIS,corrected}^{LAPs}(I_{LAPs}) -$$

$$\begin{aligned}
& \overline{\Delta\alpha_{MODIS,corrected}^{LAPs}(I_{LAPs})} + b \cdot (\Delta\alpha_{MODIS,corrected}^{LAPs}(R_{eff}) - \\
& \overline{\Delta\alpha_{MODIS,corrected}^{LAPs}(R_{eff})}) + c \cdot (\Delta\alpha_{MODIS,corrected}^{LAPs}(SD) - \\
& \overline{\Delta\alpha_{MODIS,corrected}^{LAPs}(SD)}) + d \cdot (\Delta\alpha_{MODIS,corrected}^{LAPs}(G) - \overline{\Delta\alpha_{MODIS,corrected}^{LAPs}(G)}) \quad (19)
\end{aligned}$$

where  $\Delta\alpha_{MODIS}^{LAPs,fit} - \overline{\Delta\alpha_{MODIS}^{LAPs,fit}}$  is the snow albedo reduction anomaly ( $\Delta\alpha_{MODIS,anomaly}^{LAPs,fit}$ ). Then, Eq. (19) can be written as

$$\begin{aligned}
& \Delta\alpha_{MODIS,anomaly}^{LAPs,fit} = a \cdot \Delta\alpha_{MODIS,corrected,anomaly}^{LAPs}(I_{LAPs}) + b \cdot \\
& \Delta\alpha_{MODIS,corrected,anomaly}^{LAPs}(R_{eff}) + c \cdot \Delta\alpha_{MODIS,corrected,anomaly}^{LAPs}(SD) + d \cdot \\
& \Delta\alpha_{MODIS,corrected,anomaly}^{LAPs}(G). \quad (20)
\end{aligned}$$

According to Huang and Yi (1991) and Pu et al. (2019), the fractional contribution of LAP content to the variability in snow albedo reduction ( $R_{\Delta\alpha}^{LAPs}$ ) can be calculated as:

$$R_{\Delta\alpha}^{LAPs} = \frac{1}{m} \sum_{j=1}^m \frac{(\alpha \cdot \Delta\alpha_{MODIS,corrected,anomaly}^{LAPs}(I_{LAPs})_j)^2}{K_j} \quad (21)$$

$$\begin{aligned}
K_j = & (a \cdot \Delta\alpha_{MODIS,corrected,anomaly}^{LAPs}(I_{LAPs})_j)^2 + (b \cdot \\
& \Delta\alpha_{MODIS,corrected,anomaly}^{LAPs}(R_{eff})_j)^2 + (c \cdot \Delta\alpha_{MODIS,corrected,anomaly}^{LAPs}(SD)_j)^2 + \\
& (d \cdot \Delta\alpha_{MODIS,corrected,anomaly}^{LAPs}(G)_j)^2 \quad (22)
\end{aligned}$$

where  $m$  denotes the length of the data set. Values for  $R_{\Delta\alpha}^{R_{eff}}$ ,  $R_{\Delta\alpha}^{SD}$ , and  $R_{\Delta\alpha}^G$  can be derived in the same way. Similarly, we can obtain the fractional contribution for daily radiative forcing ( $R_{RF}^{LAPs}$ ,  $R_{RF}^{R_{eff}}$ ,  $R_{RF}^{SD}$ , and  $R_{RF}^G$ ).

## 4. Results

### 4.1. Study area

1 Figure 3a depicts the ISCA employed in this study. Most are located in Eurasia, North  
2 America and the Arctic, which are dominated by grassland, shrublands and bare-soil  
3 surfaces (Fig. 3b). Several mid–high-latitude regions that typically support a deep  
4 snowpack, including southern Russia, western Europe, and eastern US, are not  
5 identified by MODIS as ISCA due to the broad distributions of forest in those areas  
6 (Fig. 3b). This pattern is supported by Bond et al. (2006), who demonstrated that, under  
7 such vegetated conditions, LAPs in snow exert a relatively minor influence on radiative  
8 forcing. On the other hand, the snowpack over midlatitude mountains at such a coarse  
9 resolution ( $0.05^\circ \times 0.05^\circ$ ) is too low to identify. In addition, midlatitude mountains are  
10 characterized as complex terrain, which will lead to high biases in radiative forcing  
11 retrieval at the coarse resolution in spite of topographic correction. Therefore, we didn't  
12 report the results over midlatitude mountains in this study.

13 As illustrated in Fig. 3a, ISCA can be separated into four general regions according to  
14 geographical distribution and pollution conditions (Fig. S2a, b): northeastern China  
15 (NEC), Eurasia (EUA), North America (NA), and the Arctic. The following analysis of  
16 snow albedo reduction and RFLS only concerns ISCA and the results mainly represent  
17 winter for midlatitudes (because spring is mostly snow-free) and spring for the Arctic  
18 (because albedos cannot be derived during polar night).

#### 19 **4.2. Global characteristics**

20 Previous studies have highlighted the dominant role of BC in light absorption by snow  
21 (Wang et al., 2013b; Dang et al., 2017). The spatial distribution of BC emissions density

1 for the Northern Hemisphere in December-May is shown in Fig. S2a. Emissions density  
2 exhibits a strong spatial inhomogeneity, ranging from  $<10^{-1}$  to  $>10^4$  g km<sup>-2</sup> month<sup>-1</sup>  
3 over ISCA. The highest values occur in NEC, where the emissions are considerably  
4 higher than EUA and NA, and the lowest values occur in the Arctic. The wet and dry  
5 deposition of BC constitute the primary mechanisms for BC accumulation in snow. As  
6 shown in Fig. S2b, the distribution of BC deposition (i.e., the sum of dry and wet  
7 deposition) is similar to BC emissions density, with the highest and lowest regional  
8 averages corresponding to NEC and the Arctic, respectively. Together, these data  
9 indicate that the NEC snowpack is heavily polluted, and thus snow albedo reduction is  
10 likely to be highest, while the Arctic snowpack is the least contaminated.

11 In addition to LAP content, the physical properties of the snowpack, such as depth and  
12 grain size, also impact snow albedo (Fig. 1). As depicted in Fig. 4a, the average  
13 snowpack in EUA (0.15 m thick) is thinner than in both NA (0.24 m) and NEC (0.19  
14 m), implying a greater impact of snow depth on snow albedo and radiative forcing in  
15 EUA. The greatest snow depths occur in the Arctic ( $>1$  m) and can be considered semi-  
16 infinite, meaning that the impact of depth on albedo and radiative forcing is negligible.  
17 Figure 4b shows the spatial distribution of MODIS-derived snow grain radius ( $R_{eff}$ ).  
18 In contrast to BC emissions density, BC deposition, and snow depth,  $R_{eff}$  exhibits  
19 minor spatial variability, with regional average values for NEC, EUA, NA, and the  
20 Arctic of 237  $\mu$ m, 227  $\mu$ m, 237  $\mu$ m, and 215  $\mu$ m, respectively. These values align with  
21 the findings of several previous studies (Painter et al., 2013; Seidel et al, 2016; Pu et

1 al., 2019) and imply that the contribution of  $R_{eff}$  to spatial variability in snow albedo  
2 reduction and radiative forcing is negligible.

3 According to Eq. (11), local solar radiation is an important factor for determining RFLS.  
4 Figure 4c depicts the December-May averaged total downward surface shortwave flux  
5 under all-sky conditions. Average solar radiative flux values for EUA and NA are  
6 comparable to one another but high relative to NEC, which lies at a generally higher  
7 latitude ( $>40^\circ$ ). The lowest values occur in the Arctic due to that region's extreme  
8 latitude. The Arctic goes through the polar night during winter, so that the radiative  
9 effect of LAPs in the Arctic mainly appears in spring. Figure S2d shows the March-  
10 May averaged downward surface shortwave flux. As can be seen that the values in the  
11 Arctic in March-May are higher than those in midlatitudes in December-February  
12 (Figure S2c). We note that snow albedo reduction and radiative forcing are only  
13 calculated over the period when snow-covered area was mapped, which implies that the  
14 RFLS will be higher in the Arctic than midlatitudes for the same snow albedo reduction.

### 15 **4.3. Corrections based on in-situ observations**

16 Albedo reduction calculated using in-situ observed LAPs ( $\Delta\alpha_{in-situ,daily}^{LAPs}$ ) were used to  
17 quantitatively correct MODIS retrievals through comparison with MODIS-retrieved  
18 snow albedo reduction ( $\Delta\alpha_{MODIS,daily}^{LAPs}$ ). Figure S4 displays scatterplots of the ratios of  
19  $\Delta\alpha_{MODIS,daily}^{LAPs}$  to  $\Delta\alpha_{in-situ,daily}^{LAPs}$  ( $r_{in-situ}^{MODIS}$ ) for each sampling sites (Ye et al., 2012;  
20 Wang et al., 2013b, 2017; Doherty et al., 2010; 2014). Briefly, for NA, EUA, and the  
21 Arctic where the snowpack is relatively clean, the values for  $r_{in-situ}^{MODIS}$  mostly range

1 between 2 and 10. In contrast, the heavily polluted snowpack in NEC returns  $r_{in-situ}^{MODIS}$   
2 values ranging from 0.5 to 2.5, indicating a negative correlation between the biases of  
3  $\Delta\alpha_{MODIS,daily}^{LAPs}$  and snow contamination, and thus supporting the findings of previous  
4 studies (Painter et al., 2012a; Pu et al., 2019). To improve the quality of MODIS  
5 retrievals, we developed the correction factors for different regions. According to Eq.  
6 (10), the correction factors for NEC, EUA, NA, Canadian Arctic, Russian Arctic and  
7 Greenland are 1.6, 4.1, 4.1, 4.4, 5.4 and 6.0, respectively. Hereafter, our analyses are  
8 based on the corrected MODIS retrievals.

9 Figure 5 compares the corrected MODIS retrievals to measurement-based results, and  
10 the mean absolute error (MAE), root mean square error (RMSE) and correlation  
11 coefficient of  $\Delta\alpha_{MODIS,corrected}^{LAPs}$  relative to  $\Delta\alpha_{in-situ,daily}^{LAPs}$  are given in Table S1.  
12 Together, these results imply that the corrected MODIS retrievals are plausible.  
13 Nevertheless, we note that the correction used in this study is spatially rough due to the  
14 low density of in-situ measurements, thus that both the uncertainty and bias are non-  
15 negligible. To address this issue, we presented further discussion about the accuracy of  
16 radiative forcing retrievals (see Sect. 4.5). We also conducted a comprehensive series  
17 of comparisons between the MODIS-derived retrievals and values provided via surface  
18 measurements, model simulations, and remote sensing (see Sect. 5). We concluded that  
19 further field-based measurements of snow albedo are required to improve the quality of  
20 satellite retrievals.

#### 21 **4.4. Spatial distributions of snow albedo reduction and radiative forcing**

1 Figure 6a shows the spatial distributions of MODIS-based albedo reduction and daily  
2 radiative forcing, and statistics are shown in Figure 6b and Table 1. On average,  
3  $\Delta\alpha_{MODIS,corrected}^{LAPs}$  and  $RF_{MODIS,daily}^{LAPs}$  provide respective values of 0.021 and 2.9 W  
4  $m^{-2}$  for Northern Hemisphere ISCA. The highest  $\Delta\alpha_{MODIS,corrected}^{LAPs}$  occurs in NEC,  
5 where the regional average of  $\sim 0.11$  exceeds those of EUA ( $\sim 0.031$ ) and NA ( $\sim 0.027$ )  
6 by a factor of  $\sim 3$ -4. This feature reflects the relatively high rate of emissions over NEC,  
7 which results in the highest level of BC deposition over ISCA (Fig. S2a, b). In contrast,  
8 being located far from major sources of pollution, the relatively clean Arctic snowpack  
9 returns the lowest  $\Delta\alpha_{MODIS,corrected}^{LAPs}$  ( $\sim 0.016$ ) of the entire Northern Hemisphere.  
10 Consistent with snow albedo reduction, the highest regional-average daily radiative  
11 forcing ( $RF_{MODIS,daily}^{LAPs}$ ) occurs in NEC, with values of  $\sim 12$  W  $m^{-2}$ , and the lowest  
12 regional average occurs in the Arctic, with values of  $\sim 2.6$  W  $m^{-2}$ . Regional-average  
13 radiative forcing for NA and EUA are both intermediate, with values of  $\sim 3.1$  W  $m^{-2}$  and  
14  $\sim 3.5$  W  $m^{-2}$ , respectively.

15 On a regional level, NEC  $\Delta\alpha_{MODIS,corrected}^{LAPs}$  falls primarily within the range  $\sim 0.077$ -  
16 0.14, and intra-regional variability is relatively small due to pervasive heavy pollution  
17 (Fig. S2). Compared to snow albedo reduction, the radiative forcing for NEC exhibits  
18 a slightly greater spatial variability due to latitude-dependent differences in the flux of  
19 surface solar radiances, ranging from  $\sim 7.2$  W  $m^{-2}$  to  $\sim 17$  W  $m^{-2}$ . In NA, where the  
20 principal ISCA are located in southern Canada, the western US, and Central America  
21 Plains,  $\Delta\alpha_{MODIS,corrected}^{LAPs}$  and  $RF_{MODIS,daily}^{LAPs}$  tend to range between  $\sim 0.014$ -0.046 and



1  $\sim 1.3\text{--}7.0 \text{ W m}^{-2}$ , respectively. In EUA,  $\Delta\alpha_{MODIS,corrected}^{LAPs}$  and  $RF_{MODIS,daily}^{LAPs}$  fall  
2 largely within the respective ranges of  $\sim 0.017\text{--}0.049$  and  $\sim 1.6\text{--}8.4 \text{ W m}^{-2}$ . Central Asia  
3 and Mongolia exhibit relatively high values for  $\Delta\alpha_{MODIS,corrected}^{LAPs}$  ( $>0.04$ ) and  
4  $RF_{MODIS,daily}^{LAPs}$  ( $>2 \text{ W m}^{-2}$ ), while this pattern likely reflects the influence of  
5 anthropogenic BC in addition to natural dust (Pu et al., 2017; Zhou et al., 2019) (Fig.  
6 S2a–b).

7 In the Arctic,  $\Delta\alpha_{MODIS,corrected}^{LAPs}$  and  $RF_{MODIS,daily}^{LAPs}$  both present quite large intra-  
8 regional variabilities from  $\sim 0.0028$  to  $\sim 0.046$  and  $\sim 0.48$  to  $6.6 \text{ W m}^{-2}$ . Greenland has  
9 the cleanest snow with  $\Delta\alpha_{MODIS,corrected}^{LAPs}$  and  $RF_{MODIS,daily}^{LAPs}$  of  $\sim 0.011\text{--}0.023$  and  
10  $\sim 0.40\text{--}3.3 \text{ W m}^{-2}$ . In Canadian Arctic,  $\Delta\alpha_{MODIS,corrected}^{LAPs}$  and  $RF_{MODIS,daily}^{LAPs}$  are  
11 mainly in a range of  $\sim 0.012\text{--}0.055$  and  $\sim 0.59\text{--}6.1 \text{ W m}^{-2}$ . In addition, the relatively high  
12 values are found around the edge of ISCA over west of Canadian Arctic. The possible  
13 reason is that these areas are suffering from faster snow melting compared with rest of  
14 Canadian Arctic in spring, which is characterized by higher snow grain size (Fig. 4b).  
15 Hence, more LAPs are accumulated in the surface snow resulting in higher snow albedo  
16 reduction. In Russian Arctic,  $\Delta\alpha_{MODIS,corrected}^{LAPs}$  and  $RF_{MODIS,daily}^{LAPs}$  values increase  
17 with altitude by  $\sim 0.012\text{--}0.048$  and  $\sim 1.0\text{--}7.3 \text{ W m}^{-2}$ . The snow albedo reduction in  
18 eastern Siberia are quite high and comparable with the values in midlatitudes. Moreover,  
19 benefiting from the higher solar radiances in eastern Siberia in Spring (Fig. S2d) than  
20 that in midlatitudes in Winter-Spring (Fig. 4c and Fig. S2c),  $RF_{MODIS,daily}^{LAPs}$  in eastern  
21 Siberia is higher than parts of midlatitudes. Even different from the findings in previous

1 modeling studies (e.g. Flanner et al., 2007; 2009), the results seem to be comparable  
2 with the limited ground-based estimates (Fig. S3). The serious biomass burning in  
3 eastern Siberia in Spring may be responsible for such high values (Warneke et al., 2010;  
4 Hegg et al., 2009). Overall, the Arctic spatial pattern of  $\Delta\alpha_{MODIS,corrected}^{LAPs}$  and  
5  $RF_{MODIS,daily}^{LAPs}$  in our study is consistent with the previous studies based on field  
6 experiments (Dang et al., 2017) and model simulation (Flanner et al., 2007).  
7 Nevertheless, we note that readers should be cautious about our reported high values in  
8 Russian Arctic and more field experiments are necessary for validating the results.

9 As mentioned above, the assumption of semi-infinite snowpack will trigger an  
10 overestimate for radiative forcing when snow depth is not thick enough. Figure 7 shows  
11 the spatial distribution of the ratio of retrieved radiative forcing using semi-infinite  
12 snow to radiative forcing using ERA-Interim snow depth. As can be seen that semi-  
13 infinite snowpack assumption will lead to an overestimate of up to ~25% in midlatitude  
14 areas, where snow depth is thin. In contrast, the influence of snow depth on radiative  
15 forcing is negligible in the Arctic, where snow is thick enough to become semi-infinite  
16 snowpack. These results demonstrated the important impact of snow depth on radiative  
17 forcing retrievals, which must be considered to reduce the overestimate for the  
18 following study.

#### 19 **4.5. Accuracy discussion**

20 In spite of the rigorous processes for radiative forcing retrieval, the uncertainty is still  
21 existed. For example, light-absorbing particles in the atmosphere will reduce the

1 accuracy of MODIS surface reflectance retrieval, even though the atmospheric  
2 correction has been conducted. In addition, previous study pointed out a high scatter  
3 when converting NDSI to FSC using Eq. (5), which will induce bias in snow albedo  
4 retrieval (Rittger et al., 2013; Riggs et al., 2016). Furthermore, the method for snow  
5 grain size retrieval is only based on a single MODIS band at 1.24  $\mu\text{m}$ , which could lead  
6 to higher uncertainties. Above all, all of these factors will result in a non-negligible  
7 uncertainty for radiative forcing retrieval, which needs to be further discussed.

8 To account for this issue, we consider that the accuracy of atmospheric correction is  
9 typically  $\pm (0.005 + 0.05 \cdot \text{reflectance})$  under conditions that AOD is less than 5.0 and  
10 solar zenith angle is less than  $75^\circ$  according to the MODIS Surface Reflectance User's  
11 Guide (Collection 6, <https://modis.gsfc.nasa.gov/data/dataproduct/mod09.php>). In  
12 addition, the bias for FSC calculation is assumed as 10% according to Riggs et al.  
13 (2016). The bias for snow grain size retrieval is assumed as 30% according to the studies  
14 of Pu et al. (2019) and Wang et al. (2017). Figure 8 shows the overall uncertainty of  
15 radiative forcing retrieval due to all these factors while Figure S6 show the uncertainty  
16 caused by each factor. In general, the upper (lower) bound of the uncertainty falls in a  
17 range of 15%~108% (-106%~-20%), with atmospheric correction and FSC calculation  
18 contributing more to the uncertainty than snow grains size retrieval. The highest  
19 uncertainty occurs in the Arctic while the lowest uncertainty occurs in NEC.  
20 Furthermore, the uncertainty shows a negative correlation with retrieved radiative  
21 forcing. The results indirectly demonstrated the reasonability of different correction

1 factors performed in different regions. For example, the value of 1.6 used in NEC  
2 suggests that the correction approach works well for heavily polluted snow, while the  
3 value of 6.0 used in Greenland for relatively clean snow suggests that the method  
4 becomes not accurate enough.

5 It is worth noting that the uncertainties from these factors could not fully explain the  
6 high correction factor in clean snow. The reason for why the ratio  $\Delta\alpha_{MODIS,daily}^{LAPs}/$   
7  $\Delta\alpha_{in-situ,daily}^{LAPs}$  to be larger than 1 is mostly like that the effect of snow surface roughness  
8 (Manninen et al., 2020) and vegetation (Pu et al., 2019). This effect is not accounted  
9 for in SNICAR, probably reduces the derived albedo from MODIS and therefore results  
10 in an overestimation of the albedo reduction attributed to LAPs. Moreover, there are  
11 other potential factors causing errors: (1) MODIS has variably spaced and discrete  
12 spectral bands and thus cannot provide a continuous spectral measurement of  
13 reflectance. This results in a non-negligible uncertainty in retrieving the radiative  
14 forcing by LAPs in snow. (Painter et al., 2012); (2) We use the retrieved radiative  
15 forcing in a pixel size of  $0.05^\circ \times 0.05^\circ$  to compare with the in-situ radiative forcing  
16 calculated from the measured  $BC_{equiv}$  concentration with a sample site located  
17 somewhere within the pixel. However, such a comparison may not be representative at  
18 some sites due to the inhomogeneous spatial distribution of LAP contents, which will  
19 influence radiative forcing retrieval; (3) In-situ measurements also have uncertainties,  
20 which may cause a high bias for snow albedo reduction in clean snow. For example, a  
21 10% bias for  $50 \text{ ng g}^{-1}$  BC can result in an 8% bias for snow albedo reduction.

## 1 **4.6. Attribution to the spatial variability of snow albedo reduction and radiative** 2 **forcing**

3 Here, we address the attributions to the spatial variability of snow albedo reduction and  
4 radiative forcing. As discussed in Sect. 3.2.5, the spatial variability in snow albedo  
5 reduction and radiative forcing are largely dependent on LAP content, snow grain radius,  
6 snow depth, and the geographic factor. Figure 9 illustrates the fractional contributions  
7 of each factor within the study regions. For the Northern Hemisphere ISCA as a whole,  
8 LAPs ( $I_{LAPs}$ ) is the greatest contributor (84.3%) to snow albedo reduction, followed by  
9  $SD$  (13.7%);  $R_{eff}$  and  $G$  have only a minor influence (1.9% and <1%, respectively)  
10 (Fig. 9a). This result confirms that the concentration of LAPs in the snowpack plays a  
11 fundamental role in spatial variability of snow albedo reduction.

12 LAPs also constitute the dominant contributors to snow albedo reduction on a regional  
13 scale, accounting for 96.0% of the Arctic signal and 56.7% in EUA and 49.9% in NA,  
14 and are the second largest contributor in NEC (40.3%). The contribution of  $SD$  is  
15 greatest in NEC (56.3%), with slightly lower values in EUA (40.3%) and NA (48.8%),  
16 reflecting the significant spatial variability in  $SD$  across these regions. In the Arctic,  
17 the snowpack is sufficiently thick to be considered a homogeneous, semi-infinite  
18 snowpack and thus the contribution of  $SD$  is negligible. In contrast,  $R_{eff}$  makes only  
19 minor contributions in NEC (3.3%), NA (1.3%), EUA (2.8%) and the Arctic (1.4%).  
20 Finally,  $G$  makes the smallest contribution to snow albedo reduction (<1%), both on  
21 regional and global scales.

1 On a hemispheric scale, the greatest contributors to radiative forcing are LAP content  
2 (70.0%) and  $G$  (22.3%), followed by  $SD$  (7.6%). As with snow albedo reduction,  
3  $R_{eff}$  plays only a minor role. The influence of  $G$  on spatial variability in radiative  
4 forcing is attributed to the high degree of variability in latitude-dependent solar  
5 radiative fluxes among ISCA. On a regional scale, the respective contributions of LAP  
6 content,  $G$ , and  $SD$  are also comparable among the four study areas, accounting for  
7 34.1%, 11.1%, and 52.0% of radiative forcing in NEC, 39.2%, 13.9%, and 46.4% in  
8 NA, and 48.0%, 19.3%, and 31.6% in EUA. The Arctic radiative forcing is dominated  
9 by LAPs (85.6%) and  $G$  (12.7%).

10 In summary, LAPs play a dominant role in the spatial variability of snow albedo  
11 reduction and radiative forcing. Our results also highlight the significant contribution  
12 of  $SD$  to snow albedo reduction and  $G$  to radiative forcing.

#### 13 **4.7. Comparisons with model simulations**

14 To investigate the global distribution and variance of RFLS, previous studies have  
15 tended to rely on Earth system models with minimal cross-checking from in-situ  
16 measurements or remote sensing observations (Qian et al., 2015; Skiles et al., 2018). In  
17 this study, we compared MODIS retrievals with CESM2 to improve our understanding  
18 of the magnitude of RFLS on a global scale.

19 Employing snow BC concentrations from CESM2, we also calculated December-May  
20 daily radiative forcing ( $RF_{CESM2}$ ) for the Northern Hemisphere ISCA during the period

1 2003–2014 (Fig. 10a). Statistics are presented in Fig. S7. Briefly,  $RF_{CESM2}$  exhibits  
2 strong spatial inhomogeneity, with values ranging from  $0.20 \text{ W m}^{-2}$  to  $5.6 \text{ W m}^{-2}$ . The  
3 highest regional average in  $RF_{CESM2}$  occurs in NEC ( $\geq 10 \text{ W m}^{-2}$ ) and the lowest in  
4 the Arctic ( $\leq 0.5 \text{ W m}^{-2}$ ), consistent with  $RF_{MODIS,daily}^{LAPs}$ .

5 Figure 10b depicts the comparison of  $RF_{MODIS,daily}^{LAPs}$  and  $RF_{CESM2}$ . In NEC,  $RF_{CESM2}$   
6 ( $15 \text{ W m}^{-2}$ ) compares well with  $RF_{MODIS,daily}^{LAPs}$  ( $12 \text{ W m}^{-2}$ ), with a significant  
7 correlation at the 99% confidence level. For EUA,  $RF_{CESM2}$  ( $3.8 \text{ W m}^{-2}$ ) is similar to  
8  $RF_{MODIS,daily}^{LAPs}$  ( $3.5 \text{ W m}^{-2}$ ). For NA,  $RF_{CESM2}$  ( $1.2 \text{ W m}^{-2}$ ) is lower than  
9  $RF_{MODIS,daily}^{LAPs}$  ( $3.1 \text{ W m}^{-2}$ ) and the spatial correlation between them are poor. In the  
10 Arctic,  $RF_{CESM2}$  is correlated with  $RF_{MODIS,daily}^{LAPs}$  at the 99% confidence level.  
11 However,  $RF_{CESM2}$  ( $1.7 \text{ W m}^{-2}$ ) is lower than  $RF_{MODIS,daily}^{LAPs}$  ( $2.6 \text{ W m}^{-2}$ ) by a factor  
12 of 1.5.

13 Overall, the RFLS derived from our MODIS retrievals and modeling-based estimates  
14 exhibit a same magnitude over the Northern Hemisphere. In NEC, the MODIS- derived  
15 and model-derived estimates show good general agreement, indicating the satisfactory  
16 performance of CESM2 in this heavily polluted region. In EUA, average radiative  
17 forcing values are comparable but the spatial correlation is relatively poor, while  
18 MODIS retrievals for the Arctic are significantly higher than those simulations.

## 19 **5. Discussion**

20 In recent decades, there has been increasing scientific interest in snow LAPs due to

1 their role in the climate system, and numerous studies have attempted to evaluate RFLS.  
2 In addition to making global-scale comparisons between our MODIS retrievals and  
3 model-based estimates, this study collects a comprehensive set of radiative forcing  
4 estimates, based on local-scale observations and remote sensing, to make quantitative  
5 regional- and global-scale comparisons and synthetically evaluate the magnitude of  
6 RFLS (Table 2). This approach also affords the opportunity to examine the MODIS  
7 retrievals used in our study.

8 Dang et al. (2017) reported RFLS values of 7–18  $\text{W m}^{-2}$ , 0.6–1.9  $\text{W m}^{-2}$ , and 0.1–0.8  
9  $\text{W m}^{-2}$  for northern China, North America, and the Arctic, respectively, which only  
10 focused on the period of January-March, and therefore are smaller than our retrievals.  
11 In NA, Sterle et al. (2013) estimated a daily-averaged RFLS of  $\sim 2.5\text{--}40 \text{ W m}^{-2}$  for the  
12 eastern Sierra Nevada in February-May, 2009, while Miller et al. (2016) reported a daily  
13 RFLS of  $\sim 35\text{--}86$  (37-100)  $\text{W m}^{-2}$  based on in-situ measurements (remote sensing) in  
14 the San Juan Mountains in May 2010. Both values are higher than our estimate ( $\sim 3.1$   
15  $\text{W m}^{-2}$ ), potentially due to the significant dust deposition in those areas.

16 We also collected the average-daily RFLS simulated by regional and/or global climate  
17 models (Table 2). For NEC, Zhao et al. (2014) and Qian et al. (2014) reported values  
18 of  $10 \text{ W m}^{-2}$  in January-February and  $5\text{--}10 \text{ W m}^{-2}$  in April, respectively. In NA, Qian  
19 et al. (2009) provided an estimate of  $3\text{--}7 \text{ W m}^{-2}$  for the central Rockies and southern  
20 Alberta in March, while Oaida et al. (2015) reported an average RFLS of  $16 \text{ W m}^{-2}$   
21 over the western US in spring. Finally, Qian et al. (2014) and Qi et al. (2017) estimated



1 RFLS values of  $<0.3 \text{ W m}^{-2}$  and  $0.024\text{--}0.39 \text{ W m}^{-2}$  for the Arctic in April, respectively.

2 We consider our retrievals for NEC to be comparable with these regional model  
3 simulations, despite some disparity. However, we note that our result is significantly  
4 lower than those of previous studies in NA, but higher in the Arctic.

5 On a global scale, Hansen and Nazarenko (2004) reported the RFLS is  $0.3 \text{ W m}^{-2}$ , while  
6 Flanner et al. (2007) showed a RFLS of  $\sim 0.05 \text{ W m}^{-2}$ . For the North Hemisphere as a  
7 whole, Bond et al. (2013) estimated a climate forcing of  $0.13 \text{ W m}^{-2}$ . Each of these  
8 previous values is significantly lower than our retrieval ( $\sim 2.9 \text{ W m}^{-2}$ ). However, those  
9 studies included all areas regardless of snow covered throughout the whole year, while  
10 our results are only for Northern Hemisphere ISCA from December to May.

11 Overall, we consider our MODIS-based retrievals to be physical realistic on both  
12 regional and global scales, although we note a number of differences between our  
13 results and those generated by different methods. On the other hand, while in-situ  
14 measurements are the most precise, their spatial coverage is restricted by logistical  
15 limitations and the extreme environments involved. Conversely, models can provide  
16 broad perspectives of climatic impacts yet are typically undermined by large uncertainty.  
17 Therefore, we argue that remote sensing provides a powerful technique, with high  
18 spatial and temporal resolutions, that can bridge the gap between in-situ measurements  
19 and climate models and reduce the uncertainties associated with the latter. Further  
20 retrieval of remote-sensing data, including the use of multiple satellites and sensors, is  
21 therefore warranted to exploit this opportunity fully. We also indicate the fact that parts

1 of central EUA and Russian Arctic, however, studies are barely performed but desired.  
2 Finally, we note that in-situ observations remain limited, and more field campaigns are  
3 needed to constrain remote sensing retrievals and modeling simulations.

## 4 **6. Conclusion**

5 We presented a global-scale evaluation of the daily radiative forcing of LAPs in the  
6 Northern Hemisphere snowpack (RFLS), estimated from remote-sensing data. The  
7 satellite-retrieved RFLS also has implications for expanding the value of limited in-situ  
8 measurements, which can provide valuable information for climate models and help  
9 optimize model simulations.

10 Based on the corrected snow albedo reduction ( $\Delta\alpha_{MODIS,corrected}^{LAPs}$ ), we calculated  
11 average-daily RFLS ( $RF_{MODIS,daily}^{LAPs}$ ) during December-May for the period 2003–2018.  
12 For the identified snow covered area over Northern Hemisphere as a whole, average  
13  $\Delta\alpha_{MODIS,corrected}^{LAPs}$  is  $\sim 0.021$  and  $RF_{MODIS,daily}^{LAPs}$  is  $\sim 2.9 \text{ W m}^{-2}$ . We also observed  
14 distinct spatial variability in snow albedo reduction and RFLS. The highest regional-  
15 average  $\Delta\alpha_{MODIS,corrected}^{LAPs}$  ( $\sim 0.11$ ) and  $RF_{MODIS,daily}^{LAPs}$  ( $\sim 12 \text{ W m}^{-2}$ ) occur in  
16 northeastern China, while the lowest regional averages of  $\sim 0.016$  and  $\sim 2.6 \text{ W m}^{-2}$ ,  
17 respectively, are observed in the Arctic. Moreover, we indicated that the semi-infinite  
18 assumption could overestimates up to  $\sim 25\%$  of RFLS, especially for thin and patchy  
19 snow, such as midlatitudes in Eurasia and NA. In addition, if the ground-based  
20 corrections were not considered, the total uncertainty of RFLS retrievals is in the range  
21 of  $15\% \sim 108\%$  ( $-106\% \sim -20\%$ ) due to atmospheric correction, snow cover fraction

1 calculation and snow grain size retrieval.

2 Following this assessment, we made quantitative attributions of the spatial variability  
3 in snow albedo reduction and radiative forcing. Our results indicate that the LAP  
4 content is the largest contributor (84.3%) to spatial variance in snow albedo reduction,  
5 followed by snow depth (13.7%), whereas snow grain size (1.9%) and the geographic  
6 factor  $G$  (<1%) are only minor contributors on a Northern Hemispheric scale. LAP  
7 content and  $G$  account for 70.0% and 22.3% of the spatial variability of radiative  
8 forcing, respectively, following by  $SD$  (7.6%) over Northern Hemisphere.

9 Retrieved RFLS values are compared spatially with the model-derived estimates of the  
10 CESM2. Our results indicate that MODIS retrievals show the same magnitude with  
11 modeled estimates for Northern Hemisphere. However, although the CESM2 perform  
12 well in NEC, there remain large uncertainties in the Arctic. To evaluate and examine  
13 the MODIS retrievals synthetically, we then compared the retrieved RFLS to previously  
14 published estimates, including local-scale observations, remote sensing retrievals, and  
15 regional- and global-scale model simulations. The results of this evaluation suggest that  
16 MODIS retrievals are generally realistic, despite a number of important differences  
17 among the various methods.

18 Finally, we urge the community to expand the ground-based measurements of the global  
19 snowpack, particularly in those regions currently lacking in-situ observations. Such  
20 development would help further constrain and improve satellite-based retrievals in the  
21 future. We propose that climate models validated by these refined remote sensing

- 1 retrievals should be able to capture the RFLS more accurately, thereby providing more
- 2 reliable estimates of the future impacts of global climate change.

1 **Data availability.**

2 MODIS data can be found at <https://earthdata.nasa.gov/> (last access: 20 January 2019).

3 CERES data can be found from NASA's Clouds and the Earth's Radiant Energy System

4 at <https://ceres.larc.nasa.gov> (last access: 12 April 2019). Shuttle Radar Topography

5 Mission (SRTM) digital elevation data are provided by the US Geological Survey at

6 <https://www.usgs.gov/> (last access: 9 December 2018). Snow depth can be found from

7 ERA-Interim at <https://www.ecmwf.int> (last access: 15 January 2019). BC emission

8 data can be found at <http://inventory.pku.edu.cn> (last access: 5 June 2019). BC

9 deposition data can be found at <https://gmao.gsfc.nasa.gov/reanalysis/MERRA-2/> (last

10 access: 5 June 2019). CMIP6 data can be found at <https://esgf-node.llnl.gov/> (last access:

11 15 July 2019). Surface measurement datasets are from Wang et al. (2013, 2017), Ye et

12 al. (2012) and Doherty et al. (2010, 2014). Springtime radiative forcing due to LAPs in

13 snow is derived from a GCM run by Flanner et al. (2007).

1 **Author contributions.**

2 PW and WX designed the study and evolved the overarching research goals and aims.  
3 CJC carried the study out and wrote the first draft with contributions from all co-authors.  
4 CJC and STL applied formal techniques such as statistical, mathematical and  
5 computational to analyze study data. ZY prepared input data and managed activities to  
6 annotate, scrub data and maintain research data. WDY completed the implementation  
7 of the computer code and supporting algorithms used for the calculations in this study.  
8 PW and WX assumed oversight and leadership responsibility for the research activity  
9 planning and execution. All authors contributed to the improvement of results and  
10 revised the final paper.

1 **Competing interests.**

2 The authors declare that they have no conflict of interest.

3 **Acknowledgments**

4 This research was supported jointly by the National Key R&D Program of China  
5 (2019YFA0606801), the National Natural Science Foundation of China (grants  
6 41975157, 41775144, and 41875091), the China Postdoctoral Science Foundation  
7 (2020M673530). We are grateful for the constructive comments and suggestions from  
8 the editor Nikos Hatzianastassiou and the referee Edward Bair as well as another  
9 anonymous referee.

1 **References**

2 Bair, E. H., Rittger, K., Skiles, S. M., and Dozier, J.: An Examination of Snow Albedo  
3 Estimates From MODIS and Their Impact on Snow Water Equivalent Reconstruction,  
4 Water Resources Research, 10.1029/2019wr024810, 2019.

5 Barnett, T. P., Adam, J. C., and Lettenmaier, D. P.: Potential impacts of a warming  
6 climate on water availability in snow-dominated regions, Nature, 438, 303-309,  
7 10.1038/nature04141, 2005.

8 Berrisford, P., Kållberg, P., Kobayashi, S., Dee, D., Uppala, S., Simmons, A. J., Poli, P.,  
9 and Sato, H.: Atmospheric conservation properties in ERA-Interim, Quarterly Journal  
10 of the Royal Meteorological Society, 137, 1381-1399, 10.1002/qj.864, 2011.

11 Bian, H., Colarco, P. R., Chin, M., Chen, G., Rodriguez, J. M., Liang, Q., Blake, D.,  
12 Chu, D. A., da Silva, A., Darmenov, A. S., Diskin, G., Fuelberg, H. E., Huey, G., Kondo,  
13 Y., Nielsen, J. E., Pan, X., and Wisthaler, A.: Source attributions of pollution to the  
14 Western Arctic during the NASA ARCTAS field campaign, Atmospheric Chemistry  
15 and Physics, 13, 4707-4721, 10.5194/acp-13-4707-2013, 2013.

16 Bond, T. C., Habib, G., and Bergstrom, R. W.: Limitations in the enhancement of visible  
17 light absorption due to mixing state, Journal of Geophysical Research, 111,  
18 10.1029/2006jd007315, 2006.

19 Bond, T. C., Doherty, S. J., Fahey, D. W., Forster, P. M., Berntsen, T., DeAngelo, B. J.,  
20 Flanner, M. G., Ghan, S., Kärcher, B., Koch, D., Kinne, S., Kondo, Y., Quinn, P. K.,



1 Sarofim, M. C., Schultz, M. G., Schulz, M., Venkataraman, C., Zhang, H., Zhang, S.,  
2 Bellouin, N., Guttikunda, S. K., Hopke, P. K., Jacobson, M. Z., Kaiser, J. W., Klimont,  
3 Z., Lohmann, U., Schwarz, J. P., Shindell, D., Storelvmo, T., Warren, S. G., and Zender,  
4 C. S.: Bounding the role of black carbon in the climate system: A scientific assessment,  
5 Journal of Geophysical Research: Atmospheres, 118, 5380-5552, 10.1002/jgrd.50171,  
6 2013.

7 Brandt, R. E., Warren, S. G., and Clarke, A. D.: A controlled snowmaking experiment  
8 testing the relation between black carbon content and reduction of snow albedo, Journal  
9 of Geophysical Research, 116, 10.1029/2010jd015330, 2011.

10 Brown, R. D., and Mote, P. W.: The Response of Northern Hemisphere Snow Cover to  
11 a Changing Climate, Journal of Climate, 22, 2124-2145, 10.1175/2008jcli2665.1, 2009.

12 Brun, E., Vionnet, V., Boone, A., Decharme, B., Peings, Y., Valette, R., Karbou, F., and  
13 Morin, S.: Simulation of Northern Eurasian Local Snow Depth, Mass, and Density  
14 Using a Detailed Snowpack Model and Meteorological Reanalyses, Journal of  
15 Hydrometeorology, 14, 203-219, 10.1175/jhm-d-12-012.1, 2013.

16 Bryant, A. C., Painter, T. H., Deems, J. S., and Bender, S. M.: Impact of dust radiative  
17 forcing in snow on accuracy of operational runoff prediction in the Upper Colorado  
18 River Basin, Geophysical Research Letters, 40, 3945-3949, 10.1002/grl.50773, 2013.

19 Chin, M., Ginoux, P., Kinne, S., Torres, O., Holben, B. N., Duncan, B. N., Martin, R.  
20 V., Logan, J. A., Higurashi, A., and Nakajima, T.: Tropospheric Aerosol Optical

1 Thickness from the GOCART Model and Comparisons with Satellite and Sun  
2 Photometer Measurements, *Journal of the Atmospheric Sciences*, 59, 461-483,  
3 10.1175/1520-0469(2002)059<0461:taotft>2.0.co;2, 2002.

4 Colarco, P., da Silva, A., Chin, M., and Diehl, T.: Online simulations of global aerosol  
5 distributions in the NASA GEOS-4 model and comparisons to satellite and ground-  
6 based aerosol optical depth, *Journal of Geophysical Research*, 115,  
7 10.1029/2009jd012820, 2010.

8 Colombo, R., Garzonio, R., Di Mauro, B., Dumont, M., Tuzet, F., Cogliati, S., Pozzi,  
9 G., Maltese, A., and Cremonese, E.: Introducing Thermal Inertia for Monitoring  
10 Snowmelt Processes With Remote Sensing, *Geophysical Research Letters*, 46, 4308-  
11 4319, 10.1029/2019gl082193, 2019.

12 Danabasoglu, G., Lamarque, J. F., Bacmeister, J., Bailey, D. A., DuVivier, A. K.,  
13 Edwards, J., Emmons, L. K., Fasullo, J., Garcia, R., Gettelman, A., Hannay, C., Holland,  
14 M. M., Large, W. G., Lauritzen, P. H., Lawrence, D. M., Lenaerts, J. T. M., Lindsay, K.,  
15 Lipscomb, W. H., Mills, M. J., Neale, R., Oleson, K. W., Otto-Bliesner, B., Phillips, A.  
16 S., Sacks, W., Tilmes, S., Kampenhout, L., Vertenstein, M., Bertini, A., Dennis, J., Deser,  
17 C., Fischer, C., Fox-Kemper, B., Kay, J. E., Kinnison, D., Kushner, P. J., Larson, V. E.,  
18 Long, M. C., Mickelson, S., Moore, J. K., Nienhouse, E., Polvani, L., Rasch, P. J., and  
19 Strand, W. G.: The Community Earth System Model Version 2 (CESM2), *Journal of*  
20 *Advances in Modeling Earth Systems*, 12, 10.1029/2019ms001916, 2020.

1 Dang, C., Brandt, R. E., and Warren, S. G.: Parameterizations for narrowband and  
2 broadband albedo of pure snow and snow containing mineral dust and black carbon,  
3 Journal of Geophysical Research: Atmospheres, 120, 5446-5468,  
4 10.1002/2014jd022646, 2015.

5 Dang, C., Warren, S. G., Fu, Q., Doherty, S. J., Sturm, M., and Su, J.: Measurements of  
6 light-absorbing particles in snow across the Arctic, North America, and China: Effects  
7 on surface albedo, J Geophys Res-Atmos, 122, 10149-10168, 2017.

8 Dee, D. P., Uppala, S. M., Simmons, A. J., Berrisford, P., Poli, P., Kobayashi, S., Andrae,  
9 U., Balmaseda, M. A., Balsamo, G., Bauer, P., Bechtold, P., Beljaars, A. C. M., van de  
10 Berg, L., Bidlot, J., Bormann, N., Delsol, C., Dragani, R., Fuentes, M., Geer, A. J.,  
11 Haimberger, L., Healy, S. B., Hersbach, H., Hólm, E. V., Isaksen, L., Kállberg, P.,  
12 Köhler, M., Matricardi, M., McNally, A. P., Monge-Sanz, B. M., Morcrette, J. J., Park,  
13 B. K., Peubey, C., de Rosnay, P., Tavolato, C., Thépaut, J. N., and Vitart, F.: The ERA-  
14 Interim reanalysis: configuration and performance of the data assimilation system,  
15 Quarterly Journal of the Royal Meteorological Society, 137, 553-597, 10.1002/qj.828,  
16 2011.

17 Deems, J. S., Painter, T. H., Barsugli, J. J., Belnap, J., and Udall, B.: Combined impacts  
18 of current and future dust deposition and regional warming on Colorado River Basin  
19 snow dynamics and hydrology, Hydrology and Earth System Sciences, 17, 4401-4413,  
20 10.5194/hess-17-4401-2013, 2013.

1 Di Mauro, B., Fava, F., Ferrero, L., Garzonio, R., Baccolo, G., Delmonte, B., and  
2 Colombo, R.: Mineral dust impact on snow radiative properties in the European Alps  
3 combining ground, UAV, and satellite observations, *Journal of Geophysical Research:*  
4 *Atmospheres*, 120, 6080-6097, 10.1002/2015jd023287, 2015.

5 Di Mauro, B., Baccolo, G., Garzonio, R., Giardino, C., Massabò, D., Piazzalunga, A.,  
6 Rossini, M., and Colombo, R.: Impact of impurities and cryoconite on the optical  
7 properties of the Morteratsch Glacier (Swiss Alps), *The Cryosphere*, 11, 2393-2409,  
8 10.5194/tc-11-2393-2017, 2017.

9 Di Mauro, B., Garzonio, R., Rossini, M., Filippa, G., Pogliotti, P., Galvagno, M., Morra  
10 di Cella, U., Migliavacca, M., Baccolo, G., Clemenza, M., Delmonte, B., Maggi, V.,  
11 Dumont, M., Tuzet, F., Lafaysse, M., Morin, S., Cremonese, E., and Colombo, R.:  
12 Saharan dust events in the European Alps: role in snowmelt and geochemical  
13 characterization, *The Cryosphere*, 13, 1147-1165, 10.5194/tc-13-1147-2019, 2019.

14 Doelling, D. R., Loeb, N. G., Keyes, D. F., Nordeen, M. L., Morstad, D., Nguyen, C.,  
15 Wielicki, B. A., Young, D. F., and Sun, M.: Geostationary Enhanced Temporal  
16 Interpolation for CERES Flux Products, *Journal of Atmospheric and Oceanic*  
17 *Technology*, 30, 1072-1090, 10.1175/jtech-d-12-00136.1, 2013.

18 Doherty, S. J., Warren, S. G., Grenfell, T. C., Clarke, A. D., and Brandt, R. E.: Light-  
19 absorbing impurities in Arctic snow, *Atmospheric Chemistry and Physics*, 10, 11647-  
20 11680, 10.5194/acp-10-11647-2010, 2010.

1 Doherty, S. J., Dang, C., Hegg, D. A., Zhang, R., and Warren, S. G.: Black carbon and  
2 other light-absorbing particles in snow of central North America, *Journal of*  
3 *Geophysical Research: Atmospheres*, 119, 12,807-812,831, 10.1002/2014jd022350,  
4 2014.

5 Dozier, J., and Marks, D.: Snow Mapping and Classification from Landsat Thematic  
6 Mapper Data, *Annals of Glaciology*, 9, 97-103,  
7 <https://doi.org/10.3189/S026030550000046X>, 1987.

8 Drusch, M., Vasiljevic, D., and Viterbo, P.: ECMWF's Global Snow Analysis:  
9 Assessment and Revision Based on Satellite Observations, *Journal of Applied*  
10 *Meteorology*, 43, 1282-1294, 10.1175/1520-0450(2004)043<1282:egsaaa>2.0.co;2,  
11 2004.

12 Eyring, V., Bony, S., Meehl, G. A., Senior, C. A., Stevens, B., Stouffer, R. J., and Taylor,  
13 K. E.: Overview of the Coupled Model Intercomparison Project Phase 6 (CMIP6)  
14 experimental design and organization, *Geosci Model Dev*, 9, 1937-1958, 10.5194/gmd-  
15 9-1937-2016, 2016.

16 Flanner, M. G., Zender, C. S., Randerson, J. T., and Rasch, P. J.: Present-day climate  
17 forcing and response from black carbon in snow, *Journal of Geophysical Research*, 112,  
18 10.1029/2006jd008003, 2007.

19 Flanner, M. G., Zender, C. S., Hess, P. G., Mahowald, N. M., Painter, T. H., Ramanathan,  
20 V., and Rasch, P. J.: Springtime warming and reduced snow cover from carbonaceous

1 particles, *Atmospheric Chemistry and Physics*, 9, 2481-2497, 10.5194/acp-9-2481-  
2 2009, 2009.

3 Flanner, M. G., Shell, K. M., Barlage, M., Perovich, D. K., and Tschudi, M. A.:  
4 Radiative forcing and albedo feedback from the Northern Hemisphere cryosphere  
5 between 1979 and 2008, *Nature Geoscience*, 4, 151-155, 10.1038/ngeo1062, 2011.

6 Flanner, M. G., Gardner, A. S., Eckhardt, S., Stohl, A., and Perket, J.: Aerosol radiative  
7 forcing from the 2010 Eyjafjallajökull volcanic eruptions, *Journal of Geophysical  
8 Research: Atmospheres*, 119, 9481-9491, 10.1002/2014jd021977, 2014.

9 Fu, Y., Zhu, J., Yang, Y., Yuan, R., Liu, G., Xian, T., and Liu, P.: Grid-cell aerosol direct  
10 shortwave radiative forcing calculated using the SBDART model with MODIS and  
11 AERONET observations: An application in winter and summer in eastern China,  
12 *Advances in Atmospheric Sciences*, 34, 952-964, 10.1007/s00376-017-6226-z, 2017.

13 Ganey, G. Q., Loso, M. G., Burgess, A. B., and Dial, R. J.: The role of microbes in  
14 snowmelt and radiative forcing on an Alaskan icefield, *Nature Geoscience*, 10, 754-759,  
15 10.1038/ngeo3027, 2017.

16 Grell, G. A., Peckham, S. E., Schmitz, R., McKeen, S. A., Frost, G., Skamarock, W. C.,  
17 and Eder, B.: Fully coupled “online” chemistry within the WRF model, *Atmospheric  
18 Environment*, 39, 6957-6975, 10.1016/j.atmosenv.2005.04.027, 2005.

19 Grenfell, T. C., Doherty, S. J., Clarke, A. D., and Warren, S. G.: Light absorption from  
20 particulate impurities in snow and ice determined by spectrophotometric analysis of

1 filters, *Appl Opt*, 50, 2037-2048, 10.1364/AO.50.002037, 2011.

2 Hadley, O. L., and Kirchstetter, T. W.: Black-carbon reduction of snow albedo, *Nature*  
3 *Climate Change*, 2, 437-440, 10.1038/nclimate1433, 2012.

4 Hall, A., and Qu, X.: Using the current seasonal cycle to constrain snow albedo  
5 feedback in future climate change, *Geophysical Research Letters*, 33,  
6 10.1029/2005gl025127, 2006.

7 Hall, D. K., Riggs, G. A., and Salomonson, V. V.: Development of methods for mapping  
8 global snow cover using moderate resolution imaging spectroradiometer data, *Remote*  
9 *Sensing of Environment*, 54, 127-140, 10.1016/0034-4257(95)00137-p, 1995.

10 Hansen, J., and Nazarenko, L.: Soot climate forcing via snow and ice albedos, *P Natl*  
11 *Acad Sci USA*, 101, 423-428, 2004.

12 Hegg, D. A., Warren, S. G., Grenfell, T. C., Doherty, S. J., Larson, T. V., and Clarke, A.  
13 D.: Source attribution of black carbon in Arctic snow, *Environ Sci Technol*, 43, 4016-  
14 4021, 10.1021/es803623f, 2009.

15 Huang, J. P. and Yi, Y. H.: Inversion of a nonlinear dynamic-model from the observation,  
16 *Sci. China Chem.*, 34, 1246–1246, 1991.

17 Huang, J., Fu, Q., Zhang, W., Wang, X., Zhang, R., Ye, H., and Warren, S. G.: Dust and  
18 Black Carbon in Seasonal Snow Across Northern China, *Bulletin of the American*  
19 *Meteorological Society*, 92, 175-181, 10.1175/2010bams3064.1, 2011.

1 Kaspari, S., Painter, T. H., Gysel, M., Skiles, S. M., and Schwikowski, M.: Seasonal  
2 and elevational variations of black carbon and dust in snow and ice in the Solu-Khumbu,  
3 Nepal and estimated radiative forcings, *Atmospheric Chemistry and Physics*, 14, 8089-  
4 8103, 10.5194/acp-14-8089-2014, 2014.

5 Kaspari, S., McKenzie Skiles, S., Delaney, I., Dixon, D., and Painter, T. H.: Accelerated  
6 glacier melt on Snow Dome, Mount Olympus, Washington, USA, due to deposition of  
7 black carbon and mineral dust from wildfire, *Journal of Geophysical Research:*  
8 *Atmospheres*, 120, 2793-2807, 10.1002/2014jd022676, 2015.

9 Lee, L. A., Reddington, C. L., and Carslaw, K. S.: On the relationship between aerosol  
10 model uncertainty and radiative forcing uncertainty, *Proc Natl Acad Sci U S A*, 113,  
11 5820-5827, 10.1073/pnas.1507050113, 2016.

12 Lewis, P., and Barnsley, M.: Influence of the sky radiance distribution on various  
13 formulations of the earth surface albedo, 6th International Symposium on Physical  
14 Measurements and Signatures in Remote Sensing, ISPRS, 1994, 707-715,

15 Liou, K. N., Takano, Y., He, C., Yang, P., Leung, L. R., Gu, Y., and Lee, W. L.:  
16 Stochastic parameterization for light absorption by internally mixed BC/dust in snow  
17 grains for application to climate models, *Journal of Geophysical Research:*  
18 *Atmospheres*, 119, 7616-7632, 10.1002/2014jd021665, 2014.

19 Loeb, N. G., Doelling, D. R., Wang, H., Su, W., Nguyen, C., Corbett, J. G., Liang, L.,  
20 Mitrescu, C., Rose, F. G., and Kato, S.: Clouds and the Earth's Radiant Energy System



1 (CERES) Energy Balanced and Filled (EBAF) Top-of-Atmosphere (TOA) Edition-4.0  
2 Data Product, *Journal of Climate*, 31, 895-918, 10.1175/jcli-d-17-0208.1, 2018.

3 Manninen, T., Anttila, K., Jääskeläinen, E., Riihelä, A., Peltoniemi, J., Räisänen, P.,  
4 Lahtinen, P., Siljamo, N., Thölix, L., Meinander, O., Kontu, A., Suokanerva, H.,  
5 Pirazzini, R., Suomalainen, J., Hakala, T., Kaasalainen, S., Kaartinen, H., Kukko, A.,  
6 Hautecoeur, O., and Roujean, J.-L.: Effect of small-scale snow surface roughness on  
7 snow albedo and reflectance, *The Cryosphere Discuss.*, [https://doi.org/10.5194/tc-](https://doi.org/10.5194/tc-2020-154)  
8 2020-154, in review, 2020.

9 Meinander, O., Kazadzis, S., Arola, A., Riihelä, A., Räisänen, P., Kivi, R., Kontu, A.,  
10 Kouznetsov, R., Sofiev, M., Svensson, J., Suokanerva, H., Aaltonen, V., Manninen, T.,  
11 Roujean, J. L., and Hautecoeur, O.: Spectral albedo of seasonal snow during intensive  
12 melt period at Sodankylä, beyond the Arctic Circle, *Atmospheric Chemistry and*  
13 *Physics*, 13, 3793-3810, 10.5194/acp-13-3793-2013, 2013.

14 Miller, S. D., Wang, F., Burgess, A. B., Skiles, S. M., Rogers, M., and Painter, T. H.:  
15 Satellite-Based Estimation of Temporally Resolved Dust Radiative Forcing in Snow  
16 Cover, *Journal of Hydrometeorology*, 17, 1999-2011, 2016.

17 Nagorski, S. A., Kaspari, S. D., Hood, E., Fellman, J. B., and Skiles, S. M.: Radiative  
18 Forcing by Dust and Black Carbon on the Juneau Icefield, Alaska, *Journal of*  
19 *Geophysical Research: Atmospheres*, 124, 3943-3959, 10.1029/2018jd029411, 2019.

20 Negi, H. S., and Kokhanovsky, A.: Retrieval of snow grain size and albedo of western

1 Himalayan snow cover using satellite data, *The Cryosphere*, 5, 831-847, 10.5194/tc-5-  
2 831-2011, 2011.

3 Nolin, A. W., and Dozier, J.: Estimating snow grain size using AVIRIS data, *Remote*  
4 *Sensing of Environment*, 44, 231-238, 10.1016/0034-4257(93)90018-s, 1993.

5 Nolin, A. W., and Dozier, J.: A Hyperspectral Method for Remotely Sensing the Grain  
6 Size of Snow, *Remote Sensing of Environment*, 74, 207-216, 10.1016/s0034-  
7 4257(00)00111-5, 2000.

8 Nowottnick, E., Colarco, P., Ferrare, R., Chen, G., Ismail, S., Anderson, B., and Browell,  
9 E.: Online simulations of mineral dust aerosol distributions: Comparisons to NAMMA  
10 observations and sensitivity to dust emission parameterization, *Journal of Geophysical*  
11 *Research*, 115, 10.1029/2009jd012692, 2010.

12 Nowottnick, E., Colarco, P., da Silva, A., Hlavka, D., and McGill, M.: The fate of  
13 saharan dust across the atlantic and implications for a central american dust barrier,  
14 *Atmospheric Chemistry and Physics*, 11, 8415-8431, 10.5194/acp-11-8415-2011, 2011.

15 Oaida, C. M., Xue, Y., Flanner, M. G., Skiles, S. M., De Sales, F., and Painter, T. H.:  
16 Improving snow albedo processes in WRF/SSiB regional climate model to assess  
17 impact of dust and black carbon in snow on surface energy balance and hydrology over  
18 western U.S, *Journal of Geophysical Research: Atmospheres*, 120, 3228-3248,  
19 10.1002/2014jd022444, 2015.

20 Painter, T. H., Roberts, D. A., Green, R. O., and Dozier, J.: The Effect of Grain Size on

1 Spectral Mixture Analysis of Snow-Covered Area from AVIRIS Data, *Remote Sensing*  
2 of Environment, 65, 320-332, 10.1016/s0034-4257(98)00041-8, 1998.

3 Painter, T. H., Barrett, A. P., Landry, C. C., Neff, J. C., Cassidy, M. P., Lawrence, C. R.,  
4 McBride, K. E., and Farmer, G. L.: Impact of disturbed desert soils on duration of  
5 mountain snow cover, *Geophysical Research Letters*, 34, 10.1029/2007gl030284, 2007.

6 Painter, T. H., Rittger, K., McKenzie, C., Slaughter, P., Davis, R. E., and Dozier, J.:  
7 Retrieval of subpixel snow covered area, grain size, and albedo from MODIS, *Remote*  
8 *Sensing of Environment*, 113, 868-879, 10.1016/j.rse.2009.01.001, 2009.

9 Painter, T. H., Deems, J. S., Belnap, J., Hamlet, A. F., Landry, C. C., and Udall, B.:  
10 Response of Colorado River runoff to dust radiative forcing in snow, *Proc Natl Acad*  
11 *Sci U S A*, 107, 17125-17130, 10.1073/pnas.0913139107, 2010.

12 Painter, T. H., Bryant, A. C., and Skiles, S. M.: Radiative forcing by light absorbing  
13 impurities in snow from MODIS surface reflectance data, *Geophysical Research*  
14 *Letters*, 39, n/a-n/a, 10.1029/2012gl052457, 2012a.

15 Painter, T. H., Skiles, S. M., Deems, J. S., Bryant, A. C., and Landry, C. C.: Dust  
16 radiative forcing in snow of the Upper Colorado River Basin: 1. A 6 year record of  
17 energy balance, radiances, and dust concentrations, *Water Resources Research*, 48,  
18 10.1029/2012wr011985, 2012b.

19 Painter, T. H., Seidel, F. C., Bryant, A. C., McKenzie Skiles, S., and Rittger, K.: Imaging  
20 spectroscopy of albedo and radiative forcing by light-absorbing impurities in mountain

1 snow, *Journal of Geophysical Research: Atmospheres*, 118, 9511-9523,  
2 10.1002/jgrd.50520, 2013.

3 Pu, W., Wang, X., Wei, H., Zhou, Y., Shi, J., Hu, Z., Jin, H., and Chen, Q.: Properties  
4 of black carbon and other insoluble light-absorbing particles in seasonal snow of  
5 northwestern China, *The Cryosphere*, 11, 1213-1233, 10.5194/tc-11-1213-2017, 2017.

6 Pu, W., Cui, J., Shi, T., Zhang, X., He, C., and Wang, X.: The remote sensing of radiative  
7 forcing by light-absorbing particles (LAPs) in seasonal snow over northeastern China,  
8 *Atmospheric Chemistry and Physics*, 19, 9949-9968, 10.5194/acp-19-9949-2019, 2019.

9 Qi, L., Li, Q., Henze, D. K., Tseng, H.-L., and He, C.: Sources of springtime surface  
10 black carbon in the Arctic: an adjoint analysis for April 2008, *Atmospheric Chemistry  
11 and Physics*, 17, 9697-9716, 10.5194/acp-17-9697-2017, 2017.

12 Qian, Y., Gustafson, W. I., Leung, L. R., and Ghan, S. J.: Effects of soot-induced snow  
13 albedo change on snowpack and hydrological cycle in western United States based on  
14 Weather Research and Forecasting chemistry and regional climate simulations, *Journal  
15 of Geophysical Research*, 114, 10.1029/2008jd011039, 2009.

16 Qian, Y., Flanner, M. G., Leung, L. R., and Wang, W.: Sensitivity studies on the impacts  
17 of Tibetan Plateau snowpack pollution on the Asian hydrological cycle and monsoon  
18 climate, *Atmospheric Chemistry and Physics*, 11, 1929-1948, 10.5194/acp-11-1929-  
19 2011, 2011.

20 Qian, Y., Wang, H., Zhang, R., Flanner, M. G., and Rasch, P. J.: A sensitivity study on

1 modeling black carbon in snow and its radiative forcing over the Arctic and Northern  
2 China, *Environmental Research Letters*, 9, 064001, 10.1088/1748-9326/9/6/064001,  
3 2014.

4 Qian, Y., Yasunari, T. J., Doherty, S. J., Flanner, M. G., Lau, W. K. M., Ming, J., Wang,  
5 H., Wang, M., Warren, S. G., and Zhang, R.: Light-absorbing particles in snow and ice:  
6 Measurement and modeling of climatic and hydrological impact, *Advances in*  
7 *Atmospheric Sciences*, 32, 64-91, 10.1007/s00376-014-0010-0, 2015.

8 Ramanathan, V., and Carmichael, G.: Global and regional climate changes due to black  
9 carbon, *Nature Geoscience*, 1, 221-227, 10.1038/ngeo156, 2008.

10 Randles, C. A., da Silva, A. M., Buchard, V., Colarco, P. R., Darmenov, A., Govindaraju,  
11 R., Smirnov, A., Holben, B., Ferrare, R., Hair, J., Shinozuka, Y., and Flynn, C. J.: The  
12 MERRA-2 Aerosol Reanalysis, 1980 Onward. Part I: System Description and Data  
13 Assimilation Evaluation, *Journal of Climate*, 30, 6823-6850, 10.1175/jcli-d-16-0609.1,  
14 2017.

15 Ricchiazzi, P., Yang, S., Gautier, C., and Sowle, D.: SBDART: A Research and Teaching  
16 Software Tool for Plane-Parallel Radiative Transfer in the Earth's Atmosphere, *Bulletin*  
17 *of the American Meteorological Society*, 79, 2101-2114, 10.1175/1520-  
18 0477(1998)079<2101:sarats>2.0.co;2, 1998.

19 Riggs G A, Hall D K, Román M O. MODIS snow products collection 6 user guide.  
20 National Snow and Ice Data Center: Boulder, CO, USA, 2016.

1 Rittger, K., Painter, T. H., and Dozier, J.: Assessment of methods for mapping snow  
2 cover from MODIS, *Advances in Water Resources*, 51, 367-  
3 380,10.1016/j.advwatres.2012.03.002, 2013.

4 Sarangi, C., Qian, Y., Rittger, K., Bormann, K. J., Liu, Y., Wang, H., Wan, H., Lin, G.,  
5 and Painter, T. H.: Impact of light-absorbing particles on snow albedo darkening and  
6 associated radiative forcing over high-mountain Asia: high-resolution WRF-Chem  
7 modeling and new satellite observations, *Atmospheric Chemistry and Physics*, 19,  
8 7105-7128, 10.5194/acp-19-7105-2019, 2019.

9 Seidel, F. C., Rittger, K., Skiles, S. M., Molotch, N. P., and Painter, T. H.: Case study  
10 of spatial and temporal variability of snow cover, grain size, albedo and radiative  
11 forcing in the Sierra Nevada and Rocky Mountain snowpack derived from imaging  
12 spectroscopy, *The Cryosphere*, 10, 1229-1244, 10.5194/tc-10-1229-2016, 2016.

13 Siegmund, A. and Menz, G.: Fernes nah gebracht–Satelliten-undLuftbildeinsatz zur  
14 Analyse von Umweltveränderungen im Geographieunterricht, *Geographie und Schule*,  
15 154, 2–10, 2005.

16 Shi, T., Pu, W., Zhou, Y., Cui, J., Zhang, D., and Wang, X.: Albedo of Black Carbon-  
17 Contaminated Snow Across Northwestern China and the Validation With Model  
18 Simulation, *Journal of Geophysical Research: Atmospheres*, 125, e2019JD032065,  
19 10.1029/2019JD032065, 2020.

20 Skamarock, W. C., Klemp, J. B., Dudhia, J., Gill, D. O., Barker, D. M., Duda, M. G.,

1 Huang, X., Wang, W., and Powers, J. G.: A description of the advanced research WRF  
2 version 3, NCAR Tech. Note, NCAR/TN-475+STR, 8 pp., Natl. Cent. for Atmos. Res.,  
3 Boulder, Colo., 2008 (available at:  
4 [http://www.mmm.ucar.edu/wrf/users/docs/arw\\_v3.pdf](http://www.mmm.ucar.edu/wrf/users/docs/arw_v3.pdf))

5 Skiles, S. M., and Painter, T.: Daily evolution in dust and black carbon content, snow  
6 grain size, and snow albedo during snowmelt, Rocky Mountains, Colorado, *J Glaciol*,  
7 63, 118-132, 10.1017/jog.2016.125, 2016.

8 Skiles, S. M., Flanner, M., Cook, J. M., Dumont, M., and Painter, T. H.: Radiative  
9 forcing by light-absorbing particles in snow, *Nature Climate Change*, 8, 964-971,  
10 10.1038/s41558-018-0296-5, 2018.

11 Solomos, S., Ansmann, A., Mamouri, R.-E., Biniotoglou, I., Patlakas, P., Marinou, E.,  
12 and Amiridis, V.: Remote sensing and modelling analysis of the extreme dust storm  
13 hitting the Middle East and eastern Mediterranean in September 2015, *Atmospheric*  
14 *Chemistry and Physics*, 17, 4063-4079, 10.5194/acp-17-4063-2017, 2017.

15 Stamnes, K., Tsay, S. C., Wiscombe, W., and Jayaweera, K.: Numerically stable  
16 algorithm for discrete-ordinate-method radiative transfer in multiple scattering and  
17 emitting layered media, *Appl Opt*, 27, 2502-2509, 10.1364/AO.27.002502, 1988.

18 Sterle, K. M., McConnell, J. R., Dozier, J., Edwards, R., and Flanner, M. G.: Retention  
19 and radiative forcing of black carbon in eastern Sierra Nevada snow, *The Cryosphere*,  
20 7, 365-374, 10.5194/tc-7-365-2013, 2013.

1 Sturm, M., Holmgren, J., and Liston, G. E.: A Seasonal Snow Cover Classification  
2 System for Local to Global Applications, *Journal of Climate*, 8, 1261-1283,  
3 10.1175/1520-0442(1995)008<1261:assccs>2.0.co;2, 1995.

4 Su, W., Corbett, J., Eitzen, Z., and Liang, L.: Next-generation angular distribution  
5 models for top-of-atmosphere radiative flux calculation from CERES instruments:  
6 validation, *Atmospheric Measurement Techniques*, 8, 3297-3313, 10.5194/amt-8-3297-  
7 2015, 2015.

8 TanrÉ, D., Deroo, C., Duhaut, P., Herman, M., Morcrette, J. J., Perbos, J., and  
9 Deschamps, P. Y.: Technical note Description of a computer code to simulate the  
10 satellite signal in the solar spectrum: the 5S code, *International Journal of Remote  
11 Sensing*, 11, 659-668, 10.1080/01431169008955048, 1990.

12 Tedesco, M., and Kokhanovsky, A. A.: The semi-analytical snow retrieval algorithm  
13 and its application to MODIS data, *Remote Sensing of Environment*, 111, 228-241,  
14 10.1016/j.rse.2007.02.036, 2007.

15 Teillet, P. M., Guindon, B., and Goodenough, D. G.: On the Slope-Aspect Correction  
16 of Multispectral Scanner Data, *Canadian Journal of Remote Sensing*, 8, 84-106,  
17 10.1080/07038992.1982.10855028, 1982.

18 Toon, O. B., McKay, C. P., Ackerman, T. P., and Santhanam, K.: Rapid calculation of  
19 radiative heating rates and photodissociation rates in inhomogeneous multiple  
20 scattering atmospheres, *Journal of Geophysical Research*, 94, 16287,



1 10.1029/JD094iD13p16287, 1989.

2 Wang, R., Tao, S., Shen, H., Wang, X., Li, B., Shen, G., Wang, B., Li, W., Liu, X.,  
3 Huang, Y., Zhang, Y., Lu, Y., and Ouyang, H.: Global emission of black carbon from  
4 motor vehicles from 1960 to 2006, *Environ Sci Technol*, 46, 1278-1284,  
5 10.1021/es2032218, 2012.

6 Wang, R., Tao, S., Ciais, P., Shen, H. Z., Huang, Y., Chen, H., Shen, G. F., Wang, B.,  
7 Li, W., Zhang, Y. Y., Lu, Y., Zhu, D., Chen, Y. C., Liu, X. P., Wang, W. T., Wang, X. L.,  
8 Liu, W. X., Li, B. G., and Piao, S. L.: High-resolution mapping of combustion processes  
9 and implications for CO<sub>2</sub> emissions, *Atmospheric Chemistry and Physics*, 13, 5189-  
10 5203, 10.5194/acp-13-5189-2013, 2013a.

11 Wang, R., Tao, S., Shen, H., Huang, Y., Chen, H., Balkanski, Y., Boucher, O., Ciais, P.,  
12 Shen, G., Li, W., Zhang, Y., Chen, Y., Lin, N., Su, S., Li, B., Liu, J., and Liu, W.: Trend  
13 in global black carbon emissions from 1960 to 2007, *Environ Sci Technol*, 48, 6780-  
14 6787, 10.1021/es5021422, 2014a.

15 Wang, X., Doherty, S. J., and Huang, J.: Black carbon and other light-absorbing  
16 impurities in snow across Northern China, *Journal of Geophysical Research:*  
17 *Atmospheres*, 118, 1471-1492, 10.1029/2012jd018291, 2013b.

18 Wang, X., Pu, W., Ren, Y., Zhang, X., Zhang, X., Shi, J., Jin, H., Dai, M., and Chen, Q.:  
19 Observations and model simulations of snow albedo reduction in seasonal snow due to  
20 insoluble light-absorbing particles during 2014 Chinese survey, *Atmospheric*

- 1 Chemistry and Physics, 17, 2279-2296, 10.5194/acp-17-2279-2017, 2017.
- 2 Wang, X., Wei, H. L., Liu, J., Xu, B. Q., Wang, M., Ji, M. X., and Jin, H. C.: Quantifying  
3 the light absorption and source attribution of insoluble light-absorbing particles on  
4 Tibetan Plateau glaciers between 2013 and 2015, *Cryosphere*, 13, 309-324, 10.5194/tc-  
5 13-309-2019, 2019.
- 6 Wang, X., Xu, B., and Ming, J.: An overview of the studies on black carbon and mineral  
7 dust deposition in snow and ice cores in East Asia, *Journal of Meteorological Research*,  
8 28, 354-370, 10.1007/s13351-014-4005-7, 2014b.
- 9 Wang, X., Zhang, X., and Di, W.: Development of an improved two-sphere integration  
10 technique for quantifying black carbon concentrations in the atmosphere and seasonal  
11 snow, *Atmospheric Measurement Techniques*, 13, 39-52, 10.5194/amt-13-39-2020,  
12 2020.
- 13 Warneke, C., Froyd, K. D., Brioude, J., Bahreini, R., Brock, C. A., Cozic, J., de Gouw,  
14 J. A., Fahey, D. W., Ferrare, R., Holloway, J. S., Middlebrook, A. M., Miller, L.,  
15 Montzka, S., Schwarz, J. P., Sodemann, H., Spackman, J. R., and Stohl, A.: An  
16 important contribution to springtime Arctic aerosol from biomass burning in Russia,  
17 *Geophysical Research Letters*, 37, n/a-n/a, 10.1029/2009gl041816, 2010.
- 18 Warren, S. G.: Optical properties of snow, *Reviews of Geophysics*, 20, 67,  
19 10.1029/RG020i001p00067, 1982.
- 20 Warren, S. G.: Impurities in Snow: Effects on Albedo and Snowmelt (Review), *Annals*

1 of *Glaciology*, 5, 177-179, 10.3189/1984AoG5-1-177-179, 1984.

2 Warren, S. G., and Brandt, R. E.: Optical constants of ice from the ultraviolet to the  
3 microwave: A revised compilation, *Journal of Geophysical Research*, 113,  
4 10.1029/2007jd009744, 2008.

5 Warren, S. G.: Can black carbon in snow be detected by remote sensing?, *Journal of*  
6 *Geophysical Research: Atmospheres*, 118, 779-786, 10.1029/2012jd018476, 2013.

7 Wiscombe, W. J., and Warren, S. G.: A Model for the Spectral Albedo of Snow. I: Pure  
8 Snow, *Journal of the Atmospheric Sciences*, 37, 2712-2733, 10.1175/1520-  
9 0469(1980)037<2712:amftsa>2.0.co;2, 1980.

10 Ye, H., Zhang, R., Shi, J., Huang, J., Warren, S. G., and Fu, Q.: Black carbon in seasonal  
11 snow across northern Xinjiang in northwestern China, *Environmental Research Letters*,  
12 7, 044002, 10.1088/1748-9326/7/4/044002, 2012.

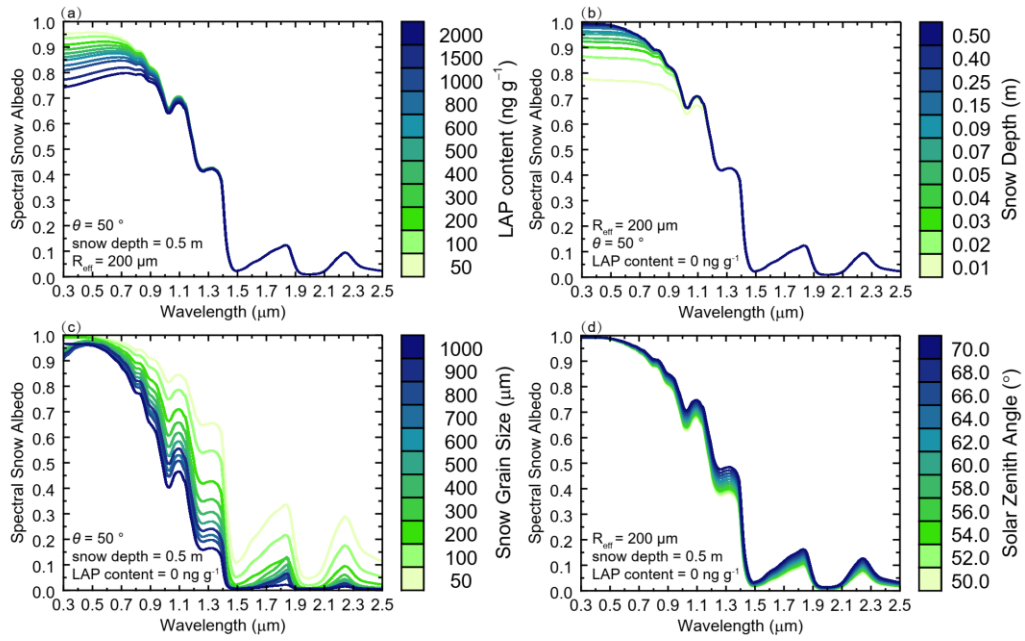
13 Zhao, C., Hu, Z., Qian, Y., Ruby Leung, L., Huang, J., Huang, M., Jin, J., Flanner, M.  
14 G., Zhang, R., Wang, H., Yan, H., Lu, Z., and Streets, D. G.: Simulating black carbon  
15 and dust and their radiative forcing in seasonal snow: a case study over North China  
16 with field campaign measurements, *Atmospheric Chemistry and Physics*, 14, 11475-  
17 11491, 10.5194/acp-14-11475-2014, 2014.

18 Zhong, E., Li, Q., Sun, S., Chen, S., and Chen, W.: Analysis of euphotic depth in snow  
19 with SNICAR transfer scheme, *Atmospheric Science Letters*, 18, 484-490,  
20 10.1002/asl.792, 2017.

1 Zhou, Y., Wen, H., Liu, J., Pu, W., Chen, Q. C., and Wang, X.: The optical characteristics  
2 and sources of chromophoric dissolved organic matter (CDOM) in seasonal snow of  
3 northwestern China, *Cryosphere*, 13, 157-175, 10.5194/tc-13-157-2019, 2019.

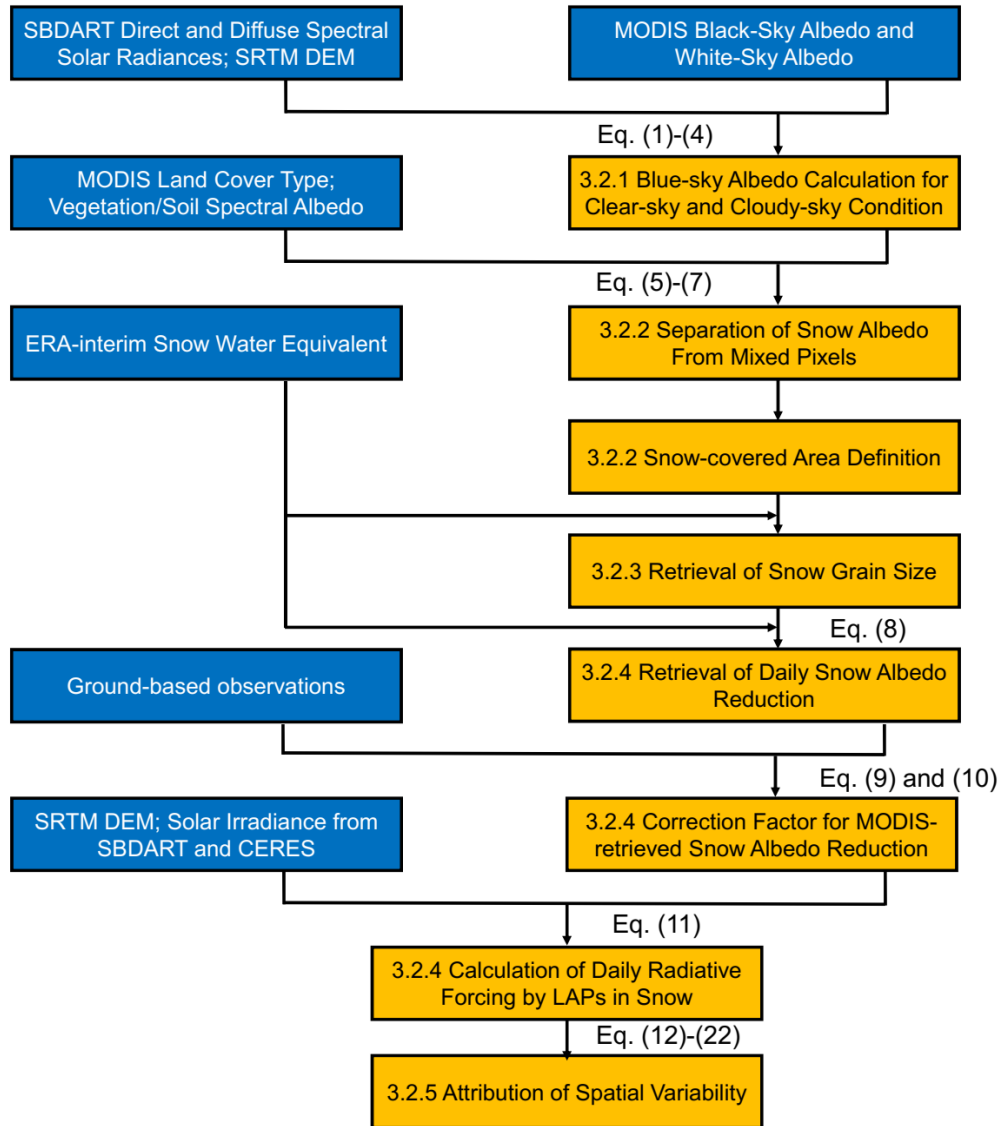
4 Zhu, C., Kobayashi, H., Kanaya, Y., and Saito, M.: Size-dependent validation of  
5 MODIS MCD64A1 burned area over six vegetation types in boreal Eurasia: Large  
6 underestimation in croplands, *Sci Rep*, 7, 4181, 10.1038/s41598-017-03739-0, 2017.

7



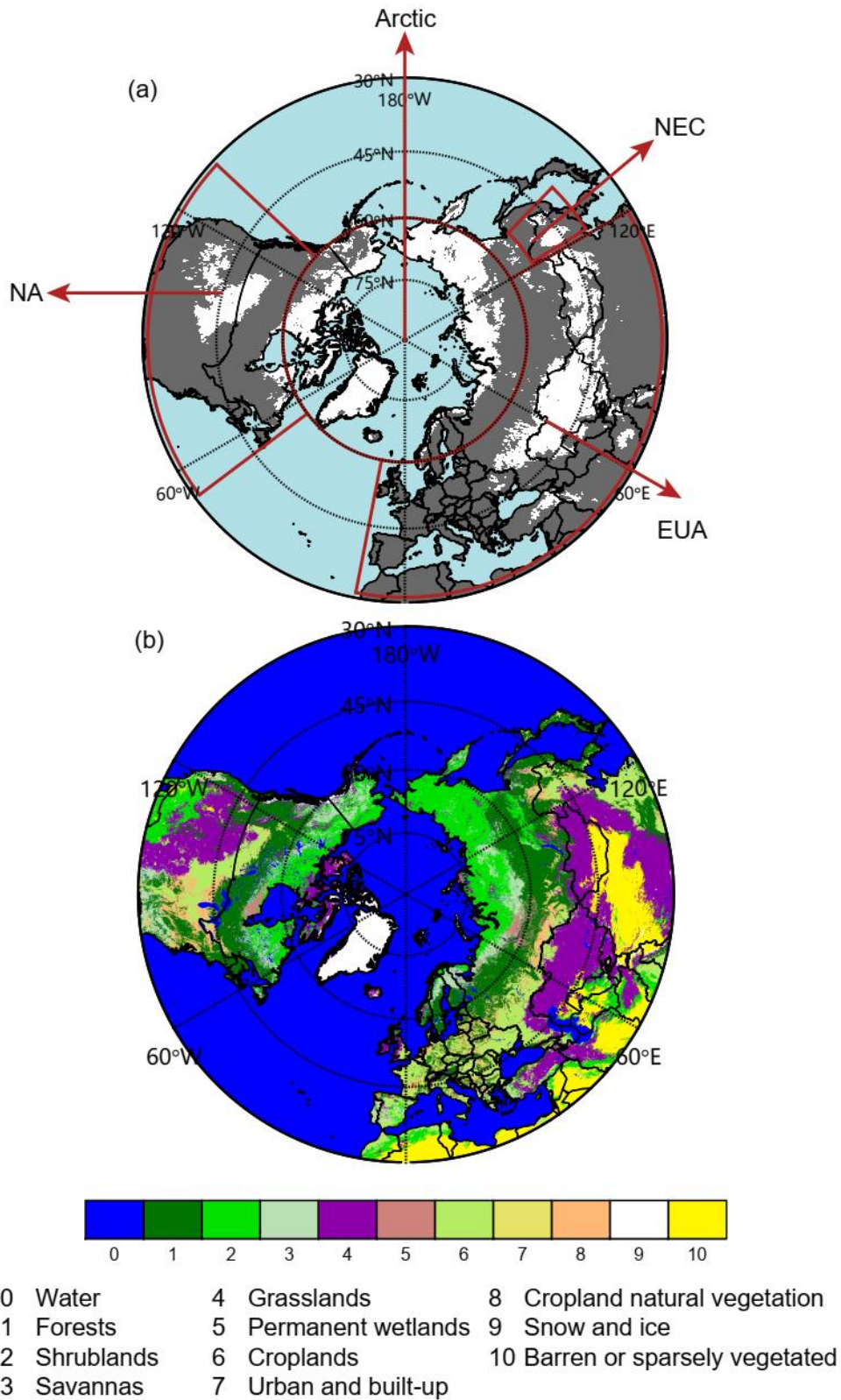
1

2 Figure 1. Variations in spectral snow albedo due to (a) LAP content ( $\text{ng g}^{-1}$ ), (b) snow depth (m), (c)  
 3 snow grain size ( $\mu\text{m}$ ), and (d) solar zenith angle (deg.) while other three parameters are kept constant.



1

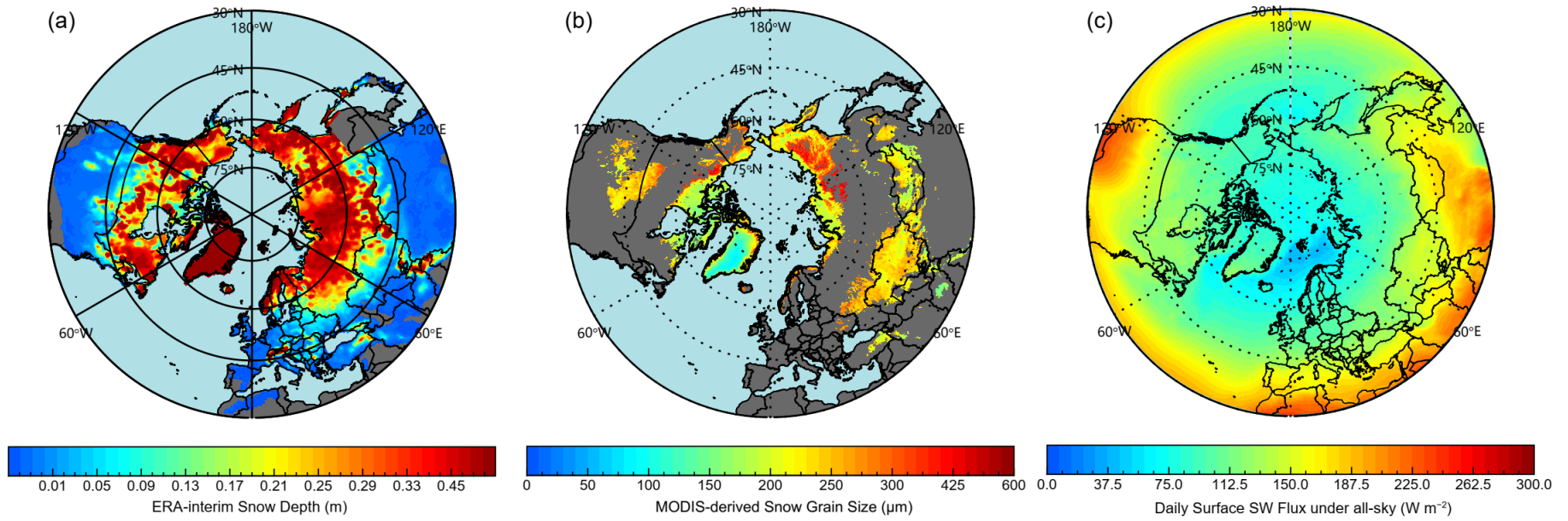
2 Figure 2. Workflow depicting the calculation and validation of radiative forcing of Laps in snow:  
 3 the blue boxes denote the external input data, while the orange boxes are used for calculations in  
 4 this study.



1

2 Figure 3. Spatial distributions of (a) identified snow-covered areas (ISCA) and (b) the different land-  
 3 cover types, based on MODIS data, for the Northern Hemisphere. ISCA (white) can be separated  
 4 into northeastern China (NEC), Eurasia (EUA), North America (NA), and the Arctic.

1

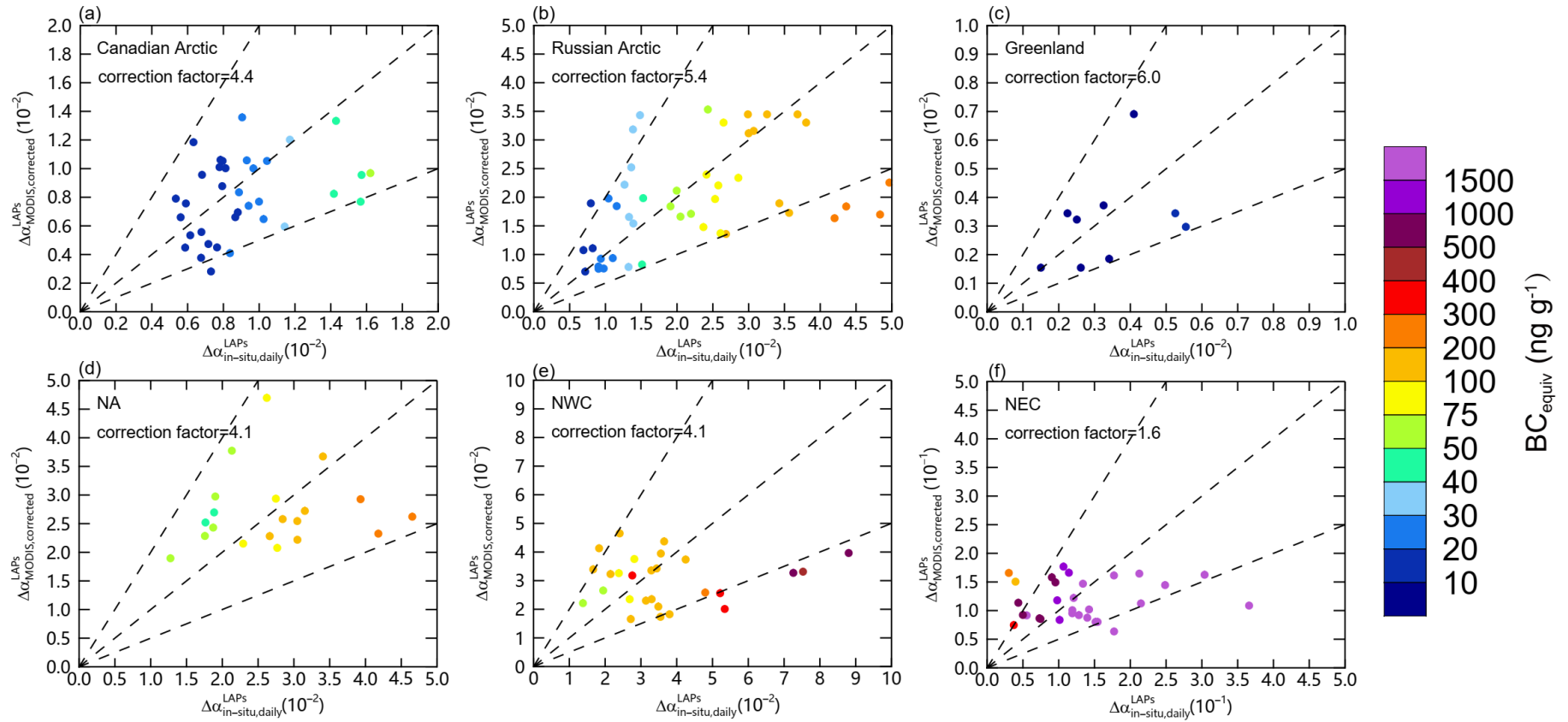


2

3 Figure 4. Spatial distributions of 2003-2018 averaged (a) snow depth from ERA-interim, (d) snow grain size retrieved by MODIS, and (c) total downward shortwave  
4 flux at the surface during December-May from CERES.



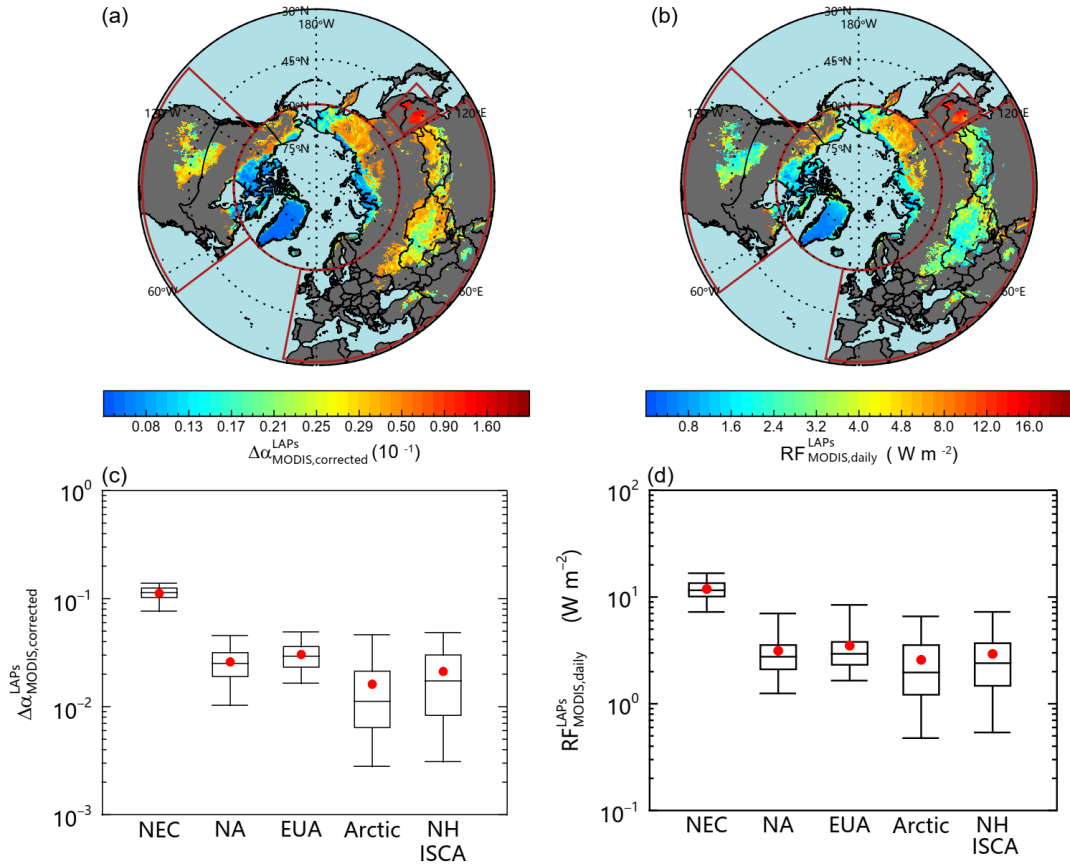
1



2

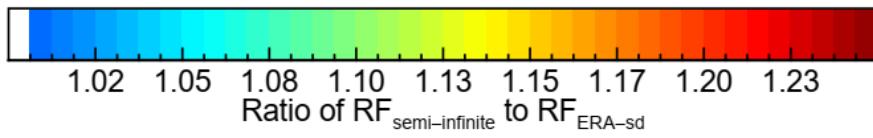
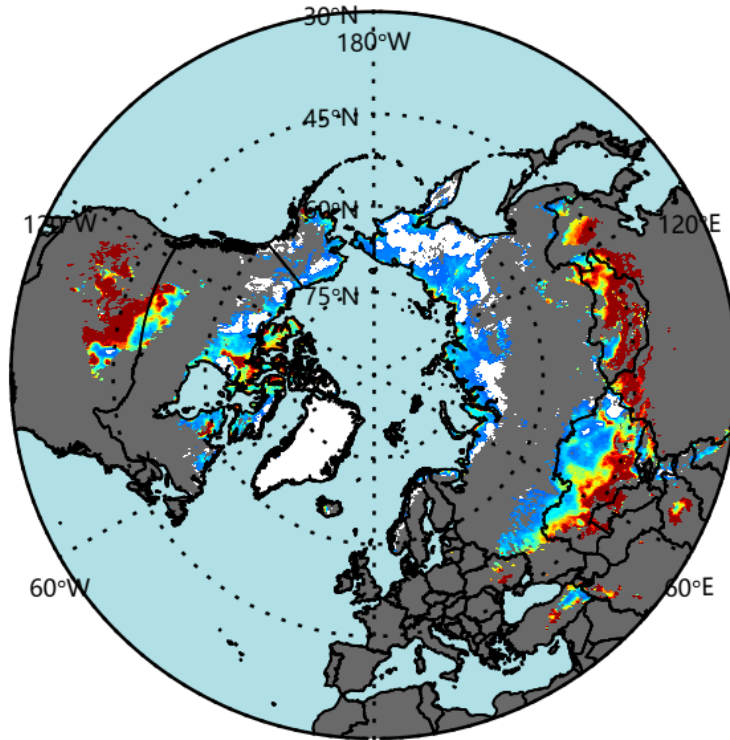
3 Figure 5. Scatterplots of  $\Delta\alpha_{MODIS,corrected}^{LAPS}$  versus  $\Delta\alpha_{in-situ,daily}^{LAPS}$ . Panels (a)–(f) represent the snow samples collected in Canadian Arctic, Russian Arctic, Greenland,  
 4 North America, Northwestern China, and Northeastern China, respectively.

1



2

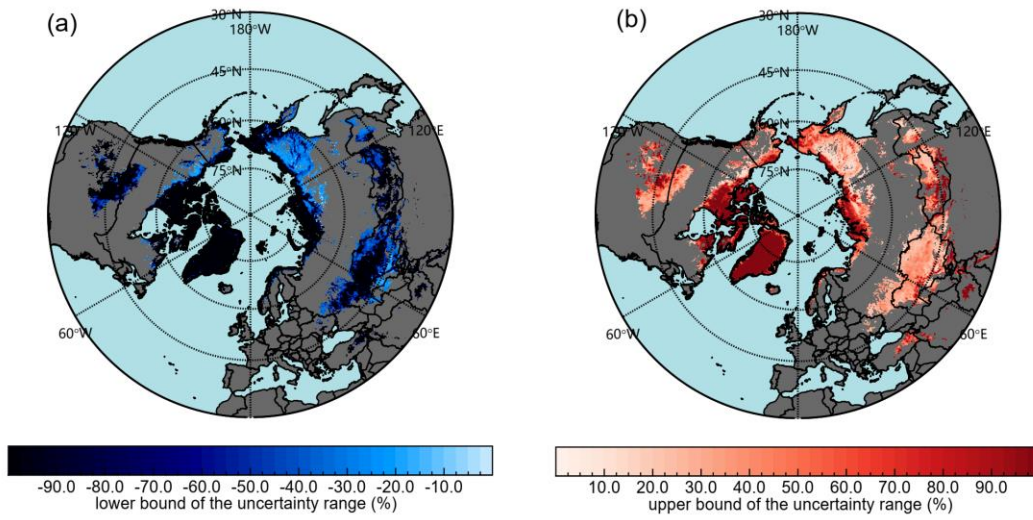
3 Figure 6. Spatial distributions of averaged (a)  $\Delta\alpha_{MODIS,corrected}^{LAPs}$ , (b)  $RF_{MODIS,daily}^{LAPs}$  and statistics  
 4 for regionally averaged (c)  $\Delta\alpha_{MODIS,corrected}^{LAPs}$  and (d)  $RF_{MODIS,daily}^{LAPs}$  for the Northern Hemisphere  
 5 ISCA in December-May during the period 2003–2018. The boxes denote the 25th and 75th quantiles,  
 6 and the horizontal lines represent the 50th quantiles (medians), the averages are shown as red dots;  
 7 the whiskers denote the 5th and 95th quantiles.



1

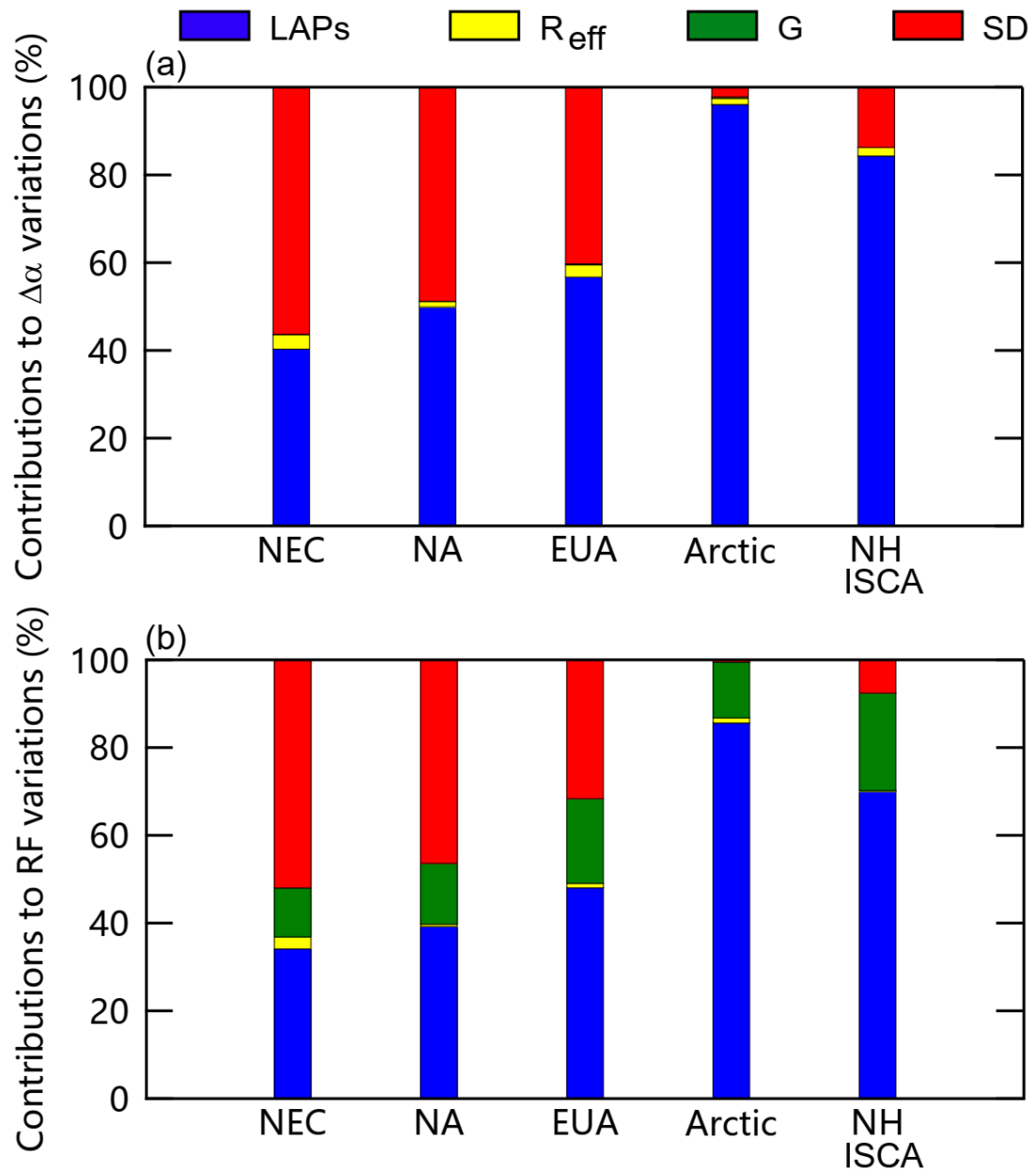
- 2 Figure 7. The spatial distribution of the ratio of retrieved radiative forcing using semi-infinite snow  
 3 to radiative forcing using ERA-Interim snow depth.

1



2

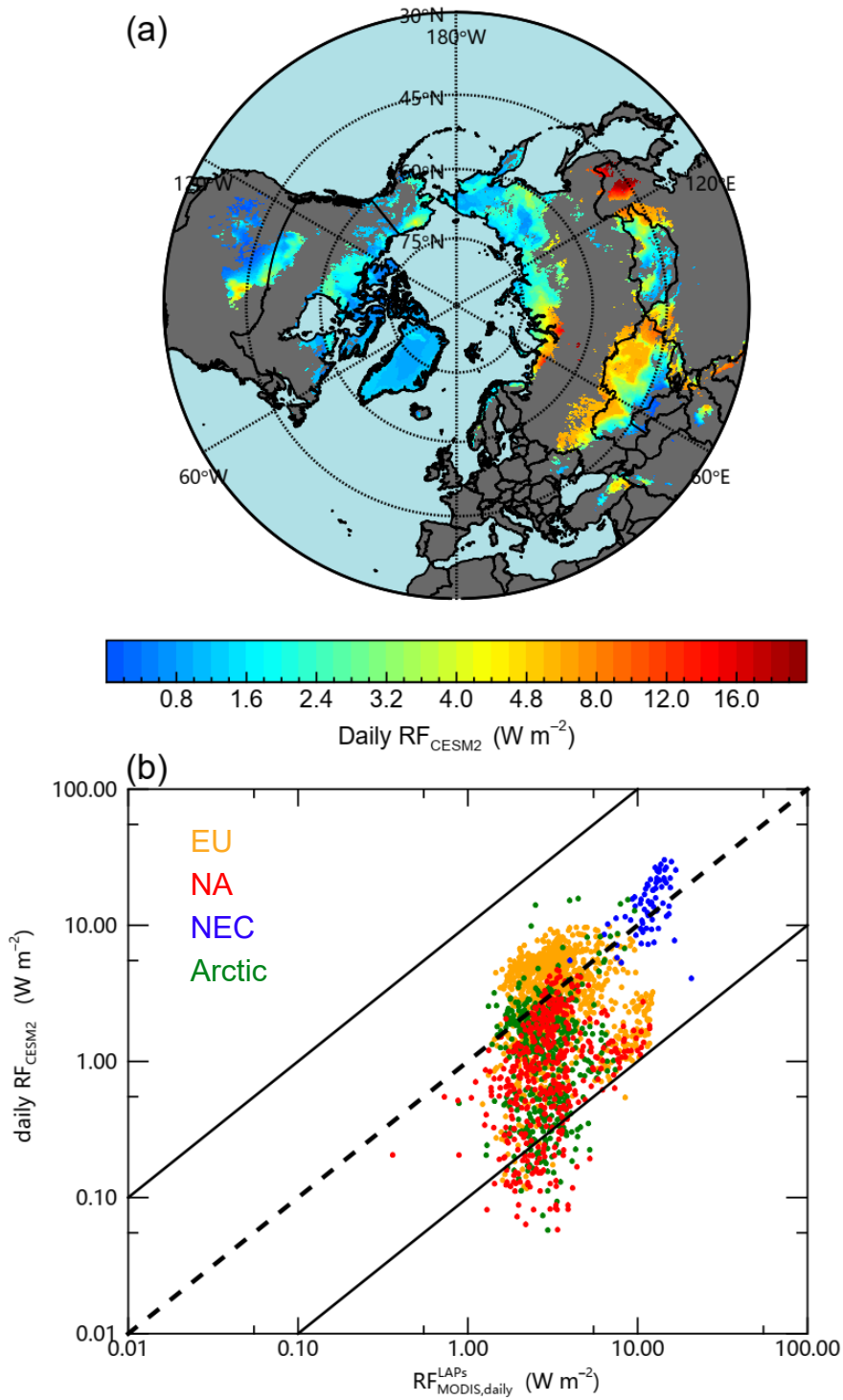
3 Figure 8. The overall lower bound and upper bound of the uncertainty range of radiative forcing  
4 retrieval due to atmospheric correction, MODIS-derived snow grain size retrieval and snow cover  
5 fraction calculation.



1

2 Figure 9. Fractional contributions of LAPs, snow grain size ( $R_{eff}$ ), geographic factor ( $G$ ), and snow

3 depth ( $SD$ ) to the spatial variations of (a) snow albedo reduction and (b) daily radiative forcing.



1

2 Figure 10. (a) Spatial distributions of average-daily radiative forcing ( $RF_{CESM2}$ ), based on the  
 3 CESM2 soot content of snow in December-May for the period 2003–2014. (b) Scatterplot of

4

$RF_{MODIS,daily}^{LAPs}$  versus  $RF_{CESM2}$ .

1

2

Table 1. Statistics for regionally averaged (5th and 95th quantiles) albedo reduction ( $\Delta\alpha_{MODIS,corrected}^{LAPs}$ ) and daily radiative forcing ( $RF_{MODIS,daily}^{LAPs}$ ,  $W m^{-2}$ )

	Northeastern China	EUA	NA	Canadian Arctic	Greenland	Russian Arctic	ISCA over Northern Hemisphere
Albedo reduction ( $\Delta\alpha_{MODIS,corrected}^{LAPs}$ )	0.11 (0.077~0.14)	0.031 (0.017~0.049)	0.027 (0.014~0.046)	0.025 (0.012~0.055)	0.016 (0.011~0.023)	0.028 (0.012~0.048)	0.021 (0.0031~0.049)
Daily radiative forcing ( $RF_{MODIS,daily}^{LAPs}$ , $W m^{-2}$ )	12 (7.2~17)	3.5 (1.6~8.4)	3.1 (1.3~7.0)	2.6 (0.59~6.1)	1.3 (0.40~3.3)	3.3 (1.0~7.3)	2.9 (0.54~7.3)

3

4

1  
2  
3

Table.2 Comparisons of radiative forcing due to LAPs in snow (this study) with observed and model-simulated values from previous studies

Study	Region	Time period	Method	Radiative forcing (W m <sup>-2</sup> )
Miller et al. (2016)	San Juan Mountains	May, 2010	Remote sensing	~37-100
Sterle et al. (2013)	eastern Sierra Nevada	Feb to May, 2009	In-situ measurements	~2.5-40
Miller et al. (2016)	San Juan Mountains	May, 2010	In-situ measurements	35-86
Dang et al. (2017)	Northern China	Jan and Feb, 2010 and 2012	In-situ measurements	7-18
	North America	Jan-Mar, 2013-2014	In-situ measurements	0.6-1.9
	The Arctic	Spring, 2005-2009	In-situ measurements	0.1-0.8
Hansen and Nazarenko (2004)	North Hemisphere		Model simulations	0.3
Qian et al. (2009)	western United States	Mar	Model simulations	~3-7
Bond et al. (2013)	Global	industrial era	Model simulations	0.13
Flanner et al. (2007)	Global	Annual 1998 (strong)	Model simulations	0.054
		Annual 2001(weak)		0.049
Qian et al. (2014)	Northeastern China	Apr	Model simulations	5-10
	North America	Apr	Model simulations	2-7



---

	The Arctic	Apr	Model simulations	<0.3
Zhao et al. (2014)	Northeastern China	Jan and Feb, 2010	Model simulations	10
Oaida et al. (2015)	western US	Spring, 2009-2013	Model simulations	16
Qi et al. (2017)	The Arctic	Apr, 2008	Model simulations	0.024-0.39
This study	Northeastern China	Dec-May, 2003-2018	Remote sensing	12
	NA			3.1
	Canadian Arctic			2.6
	Russian Arctic			3.3
	Greenland			1.3
	EUA			3.5

---